The Astrophysical Journal Supplement Series, 143:257–276, 2002 December

EMISSION LINE PROPERTIES OF ACTIVE GALACTIC NUCLEI FROM A PRE-COSTAR FAINT OBJECT SPECTROGRAPH *HUBBLE SPACE TELESCOPE* SPECTRAL ATLAS

Joanna K. Kuraszkiewicz and Paul J. Green
Harvard-Smithsonian Center for Astrophysics, 60 Garden Street, Cambridge, MA 02138;
jkuraszkiewicz@cfa.harvard.edu, pgreen@cfa.harvard.edu

Karl Forster
California Institute of Technology, 1200 East California Boulevard, MC 405-47, Pasadena, CA 91125; krl@srl.caltech.edu

Thomas L. Aldcroft and Ian N. Evans
Harvard-Smithsonian Center for Astrophysics, 60 Garden Street, Cambridge, MA 02138;
taldcroft@cfa.harvard.edu, ievans@cfa.harvard.edu

and

Anuradha Koratkar
Space Telescope Science Institute, 3700 San Martin Drive, Baltimore, MD 21218; koratkar@stsci.edu
Received 2002 April 20; accepted 2002 July 11

ABSTRACT

UV/optical emission lines offer some of the most detailed information obtainable about the intrinsic properties of quasars. Studies of the density, ionization and metal abundance of gas near the accreting black hole are probed through an intriguing but poorly understood complex of correlations between emission lines and overall quasar spectral energy distributions that has long suffered from a lack of large, consistently measured samples. As part of a broader effort to expand and systematize the data upon which these studies are built, we present measurements of the UV/optical emission line parameters in a sample of 158 active galactic nuclei observed with the Faint Object Spectrograph on the *Hubble Space Telescope* (*HST*), prior to the installation of COSTAR. We use an automated technique that accounts for galactic reddening, includes iron emission blends, galactic and intrinsic absorption lines, and performs multicomponent fits to the emission line profiles. We present measured line parameters (equivalent width and FWHM) for a large number (28) of different UV/optical lines, including upper limits for undetected lines. We also study the relations between the emission line equivalent widths and luminosity (the Baldwin effect), as well as redshift (evolution). We compare results from this *HST* FOS sample with our previous measurements of 993 QSOs in the Large Bright Quasar Survey using the same analysis technique and sum the samples to achieve better coverage of the luminosity-redshift plane. We confirm a significant Baldwin effect for UV iron emission from Green et al. and find that evolution dominates the effect for iron and for Si IV emission. The values of the Baldwin effect slopes for all UV emission lines and the dependence of the slopes on the sample's luminosity range point to a change of the SED as the cause of the Baldwin effect in the FOS sample.

Subject headings: galaxies: active — quasars: emission lines — quasars: general — ultraviolet: galaxies

On-line material: color figure, machine-readable tables

1. INTRODUCTION

The strong, broad emission lines observed in the spectra of active galactic nuclei (AGNs) are believed to form in a large number of small gas clouds photoionized by the central UV/X-ray continuum source (presumably a black hole with an accretion disk). Although it has been known from the late 1970s (see Netzer & Davidson 1979 for review) that photoionization models successfully predict the strengths of the strong UV lines, unresolved issues concerning the origin, evolution, geometry, and the acceleration mechanism of the emission line clouds persist (Krolik & Kallman 1988; Alexander & Netzer 1994; Perry & Dyson 1985; Murray & Chiang 1998; Koratkar & Gaskell 1991). In hope of solving these issues, studies of correlations among the emission lines and their relation to the continuum have been conducted. Among the most extensively examined is the anticorrelation between emission line equivalent width and luminosity called the Baldwin effect. Another intriguing set of correlations occurs between Fe II λ4570, [O III] λ5007 strength, and the FWHM and blue asymmetry of the Hβ line. Principal component analysis of measurable QSO parameters yields the principal axis of parameter variation called Eigenvector 1 (PC1; Boroson & Green 1992; Francis et al. 1992). Strong projections onto PC1 include UV spectral properties such as C III] width, Si III]/C III] ratio, C IV and N V strength (Wills et al. 1999), C IV shift/asymmetry (Marziani et al. 1996), and also soft X-ray continuum properties (Boroson & Green 1992; Laor et al. 1994, 1997).

Most studies of emission line properties to date have been conducted using large samples of nonuniform data sets compiled using emission line measurements taken from the literature (Zheng & Malkan 1993; Zamorani et al. 1992; Baldwin, Wampler, & Gaskell 1989). Such compilations often include spectra that differ significantly in quality and resolution, with emission lines measured using a variety of techniques. Most inconsistencies in the emission line measurements arise from differences in continuum placement and difficulty in estimating the amount of blended iron emission. Studies that have concentrated on uniform and consistent emission line measurements have tended to span small samples and ranges of QSO parameters (Boroson & Green 1992; Wills et al. 1999; Wilkes et al. 1999).

With the prospect of an increasing number of quasar spectra becoming available in the next few years (30,000 quasars from the 2dF and 100,000 from the SDSS surveys), there is hope that large numbers of emission line measurements will provide enough data for reliable statistical analysis, leading to an enhanced understanding of the differences in quasar emission line properties and their cause (orientation, black hole mass, accretion rate, evolution?). This goal is unlikely to be realized without an automated procedure to facilitate consistent measurements of the emission line properties from such large samples.

We have undertaken a major study of AGN spectra using a measuring technique which is largely automated. This procedure accounts for blended optical and UV iron emission, finds absorption lines and models them together with the emission lines, and provides upper limits for undetected lines. With this automated technique, we were able to consistently measure the largest single sample of QSO spectra available at the time, the Large Bright Quasar Survey (LBQS), for which 993 spectra have been modeled by Forster et al. (2001, hereafter Paper I) with the emission line properties analyzed in Green, Forster, & Kuraszkiewicz (2001, hereafter Paper II). The LBQS is a homogeneous and complete sample, with fairly low resolution (6–10 Å) and S/N (a median of ~ 5 averaged over the entire spectrum). The tight luminosity-redshift correlation in such a uniform magnitude-limited sample actually hampers disentanglement of luminosity and evolution effects (Paper II).

To broaden the power of statistical analyses of quasar properties, we have analyzed the higher S/N and resolution spectra in the archive of AGNs observed with the Faint Object Spectrograph (FOS; Keyes et al. 1995 and references therein) on board of the *Hubble Space Telescope* (*HST*). The sample is heterogeneous and extends toward lower redshifts and luminosities than the LBQS sample. In this paper, we analyze AGNs observed prior to the installation of COSTAR and present a catalog of these spectra and their emission line measurements. Spectra observed with COSTAR/FOS will be analyzed in a future paper (J. K. Kuraszkiewicz et al. 2002, in preparation).

2. THE SAMPLE

We have collected all available (UV and optical) spectrophotometric archival data for AGNs that have been observed with the FOS/*HST* prior to the installation of COSTAR in 1993 December. All spectra have been uniformly calibrated to account for temporal, wavelength- and aperture-dependent variations that are seen in the instrumental response, and combined into a preliminary pre-COSTAR Spectral Atlas (see I. N. Evans & A. P. Koratkar 2002, in preparation, for the more recent version of the Atlas, where the most up-to-date calibrating techniques were used). The average inverse sensitivity (AIS) calibration (adopted in 1996 March) was used, generated by a spline fit to the inverse sensitivities derived from an average of many observations of a number of standard stellar spectra. The AIS method for flux calibrating FOS data:

1. Normalizes count data from all apertures to the 4.″3 aperture;
2. Corrects wavelength dependent aperture throughput to account for changes in aperture throughput as a function of the optical telescope assembly focus;
3. Corrects the data for time-dependent detector sensitivity degradation;
4. Scales the data to the white dwarf model G191-B2B for photometric reference.

At this stage the sample consisted of 933 data sets and 263 objects, among which 112 targets had observations with only one grating. We included spectra taken with both high-resolution (G130H, G190H, G270H, G400H, G570H, G780H) and low-resolution (G160L, G650L) gratings. Those obtained with prism grating were excluded from the analysis, due to extremely low resolution that precludes from any reasonable emission line measurements. We have also excluded the broad absorption line (BAL) QSOs, where strong absorption features heavily disrupt the emission lines, and BL Lac objects, which spectra show no emission lines. Off-nuclear spectra were not analyzed.

To obtain a more reliable continuum fit for each object, spectra from different observations and gratings were merged together whenever the flux levels in the overlap region differed by less than 10%. When the difference in flux was larger, spectra were analyzed separately. Merged spectra were rebinned in the overlap region, in such a way that the resolution varied linearly from that of the blue disperser at the blue end of the overlap region, to that of the red disperser at the red end of the overlap region. The flux level in each wavelength bin was calculated as a weighted mean of fluxes from the two overlapping spectra at that bin. The weights changed linearly with the bin position in the overlap region, with the blue spectrum having a 100% weight and the red spectrum having 0% weight at the blue end of the overlap region, with the reverse true at the red end (for details, see I. N. Evans & A. P. Koratkar 2002, in preparation). Data obtained at different epochs were merged together in a slightly different way by rebinning the spectra in the overlap region to the lower dispersion of the two. If one of the merged spectra was particularly noisy in the overlap region, it was ignored in that region, and only the higher signal-to-noise spectrum was adopted. Finally, we removed from the sample spectra with no emission lines, whether due to low signal-to-noise or a redshift that placed strong emission lines outside the wavelength range.

3. THE CATALOG

The final list of objects includes 158 AGNs and 174 spectra and is presented in Table 1. To avoid a mélange of AGN names, including different positional and catalog designations, we use a coordinate designation based on the equinox J2000 position (in standard IAU format consisting of HHMM+/−DDMM). In addition to this, a two letter designation is used for the spectra indicating that the spectra are from a pre-COSTAR observation (*r*) and whether there is more than one spectrum of the same object (*a*–*z*), e.g., NGC 3031, which has a J2000 position designation of 0955+6903 has three pre-COSTAR spectra 0955+6903ra, 0955+6903rb, and 0955+6903rc (which have not been merged due to differing flux levels). A capital letter at the end of the name indicates that the object is a gravitational lens and that separate spectra of each lensed component were observed and analyzed, e.g., 1230+1223rA, 1230+1223rB.

TABLE 1

LIST OF OBJECTS AND SPECTRA

Designation	Name	Type[a]	Redshift	N_H[b]	Spectra
0005+1609.....	PKS 0003+15	Q	0.450	3.87	0005+1609ra
0010+1058.....	III Zw 2	S1	0.089	5.90	0010+1058ra
0027+2241.....	NAB 0024+22	Q	1.119	3.73	0027+2241ra
0047+0319.....	PKS 0044+030	Q	0.623	2.81	0047+0319ra
0053+1241.....	I Zw 1	Q	0.061	5.07	0053+1241ra
0054+2525.....	0052+2509	S1	0.155	4.38	0054+2525ra
0103+0221.....	0100+0205	Q	0.393	2.40	0103+0221ra
0113+2958.....	B2 0110+29	Q	0.363	6.04	0113+2958ra
0115−0127.....	PKS 0112−017	Q	1.365	5.37	0115−0127ra
0118+0258.....	0115+027	Q	0.672	3.51	0118+0258ra
0123−5848.....	Fairall 9	S1	0.047	3.19	0123−5848ra
0125−0005.....	PKS 0122−00	Q	1.070	3.25	0125−0005ra
0136+2057.....	3C 47	Q	0.425	5.12	0136+2057ra
0242−0000.....	NGC 1068	S2	0.004	2.95	0242−0000ra, 0242−0000rb
0256−0126.....	0253−0138	Q	0.879	5.60	0256−0126ra
0319+4130.....	NGC 1275	S2	0.018	13.93	0319+4130ra
0323−4930.....	RX J03233−4931	Q	0.071	1.73	0323−4930ra
0336−3607.....	0334−3617	Q	1.100	1.40	0336−3607ra
0351−1429.....	3C 95	Q	0.616	4.20	0351−1429ra
0352−0711.....	0350−0719	Q	0.962	5.78	0352−0711ra
0357−4812.....	PKS 0355−48	Q	1.005	1.16	0357−4812ra
0405−1308.....	PKS 0403−13	Q	0.571	4.24	0405−1308ra
0407−1211.....	PKS 0405−12	Q	0.573	3.66	0407−1211ra
0417−0553.....	PKS 0414−06	Q	0.775	4.34	0417−0553ra
0420−5456.....	NGC 1566	S1	0.005	1.35	0420−5456ra
0441−4313.....	PKS 0439−433	Q	0.593	1.30	0441−4313ra
0456−2159.....	PKS 0454−22	Q	0.533	2.77	0456−2159ra
0506−6109.....	0506−6113	Q	1.093	2.53	0506−6109ra
0615+7102.....	Mrk 3	S2	0.014	8.76	0615+7102ra
0630+6905.....	HS 0624+6907	Q	0.370	6.38	0630+6905ra, 0630+6905rb
0635−7516.....	PKS 0637−75	Q	0.653	9.22	0635−7516ra
0713+1146.....	3C 175	Q	0.770	11.51	0713+1146ra
0743−6726.....	PKS 0743−67	Q	1.510	11.91	0743−6726ra
0744+3753.....	3C 186	Q	1.063	4.87	0744+3753ra
0745+3142.....	B2 0742+31	Q	0.461	5.12	0745+3142ra
0755+2542.....	OI 287	Q	0.446	4.54	0755+2542ra
0837+4450.....	WSTB 55W 037	S2	0.208	3.00	0837+4450ra
0840+1312.....	3C 207	Q	0.681	5.40	0840+1312ra
0847+3445.....	Ton 951	Q	0.064	3.32	0847+3445ra
0853+4349.....	US 1867	Q	0.514	2.62	0853+4349ra
0859+4637.....	0856+4649	Q	0.924	2.30	0859+4637ra
0902−1415.....	PKS 0859−14	Q	1.327	5.92	0902−1415ra
0906+1646.....	3C 215	Q	0.412	3.75	0906+1646ra
0909+4253.....	3C 216	Q	0.670	1.39	0909+4253ra
0919+5106.....	NGC 2841 UB3	Q	0.556	1.29	0919+5106ra
0927+3902.....	B2 0923+392	Q	0.695	1.61	0927+3902ra, 0927+3902rb
0955+6903.....	NGC 3031	S1.8	−0.0001	4.34	0955+6903ra, 0955+6903rb, 0955+6903rc
0956+4115.....	PG 0953+414	Q	0.234	1.12	0956+4115ra
0957+5522.....	4C 55.17	Q	0.909	0.88	0957+5522ra
0958+3224.....	0955+326	Q	0.531	1.77	0958+3224ra
1003+6813.....	0959+68W1	Q	0.773	3.75	1003+6813ra
1004+2855.....	Ton 28	Q	0.330	1.85	1004+2855ra
1010+4132.....	4C 41.21	Q	0.612	1.13	1010+4132ra
1011+1304.....	PG 1008+133	Q	1.287	3.72	1011+1304ra
1013+3551.....	CSO 251	Q	0.070	1.24	1013+3551ra
1024+1912.....	4C 19.34	Q	0.828	2.42	1024+1912ra
1041+0610.....	4C 06.41	Q	1.270	2.82	1041+0610ra
1042+1203.....	3C 245.0	Q	1.029	2.70	1042+1203ra
1048−2509.....	NGC 3393	S2	0.012	5.89	1048−2509ra
1051−0051.....	PG 1049−005	Q	0.360	4.21	1051−0051ra
1058+1951.....	PKS 1055+20	Q	1.110	1.89	1058+1951ra
1104+7658.....	3C 249.1	Q	0.312	2.87	1104+7658ra
1106−0052.....	PKS 1103−006	Q	0.423	4.20	1106−0052ra
1107+1628.....	MC 1104+167	S1	0.632	1.42	1107+1628ra
1114+4037.....	3C 254	Q	0.734	1.75	1114+4037ra

TABLE 1—*Continued*

Designation	Name	Type[a]	Redshift	N_H[b]	Spectra
1119+2119.....	PG 1116+215	Q	0.177	1.40	1119+2119ra
1125+5910.....	1123+5926	Q	0.858	0.87	1125+5910ra
1130−1449.....	PKS 1127−14	Q	1.187	3.83	1130−1449ra
1132+1023.....	1130+106Y	Q	0.504	2.88	1132+1023ra
1139+6547.....	3C 263	Q	0.646	0.91	1139+6547ra
1139−1350.....	PKS 1136−13	Q	0.560	3.55	1139−1350ra
1139−3744.....	NGC 3783	S1	0.009	9.59	1139−3744ra
1151+5437.....	PG 1148+549	Q	0.969	0.96	1151+5437ra
1158+6254.....	1156+6311	Q	0.594	1.67	1158+6254ra
1204+2754.....	GQ Comae	Q	0.165	1.76	1204+2754ra
1208+4540.....	PG 1206+459	Q	1.158	1.11	1208+4540ra
1210+0954.....	1208+101A, B	Q	3.822	1.59	1210+0954rA, 1210+0954rB
1210+3924.....	NGC 4151	S1	0.003	2.17	1210+3924ra, 1210+3924rb, 1210+3924rc
1214+1403.....	PG 1211+143	Q	0.081	2.76	1214+1403ra
1219+0638.....	PG 1216+069	Q	0.331	1.56	1219+0638ra
1221+7518.....	Mrk 205	S1	0.071	2.74	1221+7518ra, 1221+7518rb
1225+3332.....	NGC 4395	S1.8	0.001	1.43	1225+3332ra
1229+0203.....	PG 1226+023	Q	0.158	1.68	1229+0203ra
1230+1223.....	NGC 4486A, B	Q	0.004	2.51	1230+1223rA, 1230+1223rB
1231−0224.....	PKS 1229−02	Q	1.045	2.34	1231−0224ra
1233+0931.....	Q1230+0947	Q	0.415	1.57	1233+0931ra
1244+1721.....	PG 1241+176	Q	1.273	1.93	1244+1721ra
1247+3209.....	B2 1244+32B	Q	0.949	1.27	1247+3209ra
1252+5634.....	3C 277.1	Q	0.321	1.03	1252+5634ra
1254+1141.....	PKS 1252+119	Q	0.871	2.55	1254+1141ra
1256−0547.....	3C 279	Q	0.536	2.22	1256−0547ra
1259+3423.....	B201 1257+346	Q	1.375	1.13	1259+3423ra
1301+5902.....	PG 1259+593	Q	0.462	1.54	1301+5902ra
1305−1033.....	PKS 1302−102	Q	0.278	3.26	1305−1033ra, 1305−1033rb
1308+3005.....	1306+3021	Q	0.806	1.04	1308+3005ra
1309+0819.....	1307+0835	S1	0.155	2.13	1309+0819ra
1319+2728.....	Ton 153	Q	1.022	1.27	1319+2728ra
1319+5148.....	1317+5203	Q	1.060	1.26	1319+5148ra
1323+2910.....	Ton 157	Q	0.960	1.17	1323+2910ra
1331+3030.....	3C 286.0	Q	0.849	1.14	1331+3030ra
1336+1725.....	PG 1333+176	Q	0.553	1.71	1336+1725ra
1341+4123.....	PG 1338+416	Q	1.219	0.76	1341+4123ra
1342+6021.....	3C 288.1	Q	0.961	2.09	1342+6021ra
1343+2844.....	B2 1340+29	Q	0.905	1.19	1343+2844ra
1349+5341.....	4C 53.28	Q	0.980	1.19	1349+5341ra
1354+0052.....	PG 1352+011	Q	1.117	2.07	1354+0052ra
1357+1919.....	PKS 1354+19	Q	0.720	2.90	1357+1919ra
1358+5752.....	4C 58.29	Q	1.371	1.29	1358+5752ra
1359−4152.....	1355−4138	Q	0.313	5.57	1359−4152ra
1404+0937.....	1401+0951	Q	0.441	1.95	1404+0937ra
1405+2555.....	PG 1402+261	Q	0.164	1.40	1405+2555ra
1409+2618.....	PG 1407+265	Q	0.940	1.36	1409+2618ra
1417+2508.....	NGC 5548	S1	0.017	1.61	1417+2508ra, 1417+2508rb
1417+4456.....	PG 1415+451	Q	0.114	0.96	1417+4456ra
1418+1703.....	MC 1415+172	Q	0.821	1.63	1418+1703ra
1427+1949.....	1425+2003	S1	0.113	2.46	1427+1949ra
1427−1203.....	PKS 1424−11	Q	0.806	7.88	1427−1203ra
1436+6336.....	S4−1435+63	Q	2.068	1.57	1436+6336ra
1437−0147.....	Q1435−0134	Q	1.310	3.66	1437−0147ra
1442+3526.....	Mrk 478	S1	0.079	0.96	1442+3526ra
1446+4035.....	PG 1444+407	Q	0.267	1.08	1446+4035ra
1454−3747.....	PKS 1451−375	Q	0.314	6.24	1454−3747ra
1514+3650.....	B2 1512+37	S1	0.371	1.40	1514+3650ra
1524+0958.....	PG 1522+101	Q	1.321	2.67	1524+0958ra
1539+4735.....	PG 1538+477	Q	0.772	1.62	1539+4735ra, 1539+4735rb
1547+2052.....	3CR 323.1	Q	0.264	4.04	1547+2052ra
1557+3304.....	B2 1555+33	Q	0.942	2.57	1557+3304ra
1613+3412.....	DA 406	Q	1.401	1.44	1613+3412ra
1614+2604.....	1612+2611	S1	0.131	3.77	1614+2604ra
1620+1736.....	3C 334	Q	0.555	4.07	1620+1736ra, 1620+1736rb
1633+3924.....	1631+3930	Q	1.023	0.92	1633+3924ra

TABLE 1—*Continued*

Designation	Name	Type[a]	Redshift	N_H[b]	Spectra
1634+7031.....	PG 1634+706	Q	1.334	5.47	1634+7031ra
1638+5720.....	OHIO S 562	Q	0.751	1.77	1638+5720ra
1642+3948.....	3C 345	Q	0.593	0.89	1642+3948ra
1658+0515.....	PKS 1656+053	Q	0.879	6.11	1658+0515ra
1704+6044.....	3C 351	Q	0.372	2.02	1704+6044ra
1719+4804.....	PG 1718+481	Q	1.084	2.11	1719+4804ra
1821+6420.....	E1821+643	S1	0.297	3.81	1821+6420ra
1927+7358.....	4C 73.18	Q	0.302	7.24	1927+7358ra
2044−1043.....	MRK 509	S1	0.034	4.44	2044−1043ra
2114+0607.....	PG 2112+059	Q	0.466	6.26	2114+0607ra
2131−1207.....	PKS 2128−12	Q	0.501	4.77	2131−1207ra
2137−1432.....	PKS 2135−147	Q	0.200	4.45	2137−1432ra
2143+1743.....	OHIO X 169	Q	0.211	8.21	2143+1743ra
2148+0657.....	PKS 2145+06	Q	0.990	4.70	2148+0657ra
2203+3145.....	B2 2201+315 A	Q	0.295	5.00	2203+3145ra
2218−0335.....	PKS 2216−03	Q	0.901	6.18	2218−0335ra, 2218−0335rc
2225−0457.....	3C 446	Q	1.404	5.26	2225−0457ra
2232+1143.....	CTA 102	Q	1.037	5.05	2232+1143ra
2246−1206.....	PKS 2243−123	Q	0.630	4.58	2246−1206ra
2253+1608.....	3C 454.3	Q	0.859	6.94	2253+1608ra, 2253+1608rb
2254+1136.....	4C 11.72	Q	0.326	5.42	2254+1136ra
2303−6807.....	PKS 2300−683	Q	0.512	2.65	2303−6807ra
2311+1008.....	PG 2308+098	Q	0.433	3.81	2311+1008ra
2342−0322.....	PKS 2340−036	Q	0.896	3.55	2342−0322ra
2346+0930.....	PKS 2344+09	Q	0.677	4.90	2346+0930ra
2351−0109.....	2349−0125	S1	0.174	3.22	2351−0109ra
2355−3357.....	PKS 2352−34	Q	0.706	1.06	2355−3357ra

NOTE.—Table 1 is also available in machine-readable form in the electronic edition of the *Astrophysical Journal Supplement*.

[a] Q, QSO; S1, Seyfert 1; S2, Seyfert 2.

[b] N_H is in units of 10^{20} cm^{-2}.

4. ANALYSIS OF THE SPECTRA

The analysis of the spectra follows the procedure described in Paper I, which modeled spectra of the LBQS sample. Small adjustments, however, have been made to accommodate the FOS spectra (see below). The modeling software "Sherpa" (Freeman, Doe, & Siemiginowska 2001), developed for the *Chandra* mission, was used, where the model parameters were determined from a minimization of the χ^2 statistic with modified calculation of uncertainties in each bin (Gehrels 1986) and using the Powell optimization method. The procedure begins with fitting a power-law continuum to regions of the spectrum redward of Lyα that are uncontaminated by emission lines and away from blended iron emission. The continuum windows used are presented in Table 2 and are the same as those in Paper I with one minor exception. In four cases (0351−1429ra, 0958+3224ra, 1010+4132ra, 1107+1628ra) we added an additional continuum window at the red side of C III] λ1909 to better constrain the continuum. In most cases one power law was sufficient. However, in a small number of cases (see Appendix), where the spectra covered a large wavelength range (both UV and optical), a second power law, extending redward of $\lambda_{rest} = 4200$ Å was introduced. A Galactic reddening correction was applied to the power-law continua following the prescription of Cardelli, Clayton, & Mathis (1989; see Paper I for details), where the neutral hydrogen column density (N_H in units of 10^{20} cm^{-2}) used for each object is given in Table 1. The values are mostly taken

TABLE 2

CONTINUUM AND IRON FITTING WINDOWS

REST FRAME WAVELENGTH RANGE (Å)		EMISSION LINES NEARBY	
Continuum	Iron	Blueward	Redward
1140–1150[a]		O VI λ1035	Lyα λ1215
1275–1280[b]		N V λ1243	O I λ1305
1320–1330		O I λ1305	Si IV + O IV] λ1400
1455–1470		Si IV + O IV] λ1400	C IV λ1549
1690–1700		He II λ1640	Al III λ1859
2160–2180	2020–2120		
2225–2250	2250–2650	C III] λ1909	Mg II λ2800
3010–3040[c]	2900–3000		
3240–3270		Mg II λ2800	[Ne V] λ3426
3790–3810		[O II] λ3728	[Ne III] λ3869
4210–4230		Hδ λ4102	Hγ λ4340
	4400–4750[d]	[O III] λ4363	Hβ λ4861
5080–5100	5150–5500		
5600–5630		[O III] λ5007	He I λ5876
5970–6000		He I λ5876	[N II] λ6549

NOTES.—In three cases: 0351−1429ra, 0958+3224ra, and 1010+4132ra, 1107+1628ra an additional continuum window was added redward of C III] at 2000–2020 Å rest frame, to obtain a better power-law continuum fit. In the Lyβ + O VI region a flat "pseudo" continuum was fitted to the following continuum windows: 980–1010 Å and 1060–1090 Å rest frame.

[a] This window lies on the blue side of the Lyα emission line and is only used where no other continuum window is available.

[b] This window is used only when windows at larger wavelength are unavailable.

[c] May have some iron emission contamination.

[d] He II λ4686 lies in this window.

from the Bell Laboratory H I survey (Stark et al. 1992). However, for a few AGNs for which N_H had been specifically measured, we quote the values from the literature (Lockman & Savage 1995; Elvis, Wilkes, & Lockman 1989), and for objects with declination $>40°$, N_H is from Heiles & Cleary (1979).

The next step was to model the blended iron emission, which is particularly strong around Mg II, Hβ and redward of C III]. We use the UV template of Vestergaard & Wilkes (2001) covering 1250 Å $< \lambda_{rest} <$ 3100 Å and the optical template from Boroson & Green (1992), covering 4400 Å $< \lambda_{rest} <$ 7000 Å. The iron template spectrum was broadened by convolving with Gaussian functions of widths between 900 km s^{-1} and 10,000 km s^{-1} and separated by steps of 250 km s^{-1}, while conserving the total flux in each template. The strengths of the iron emission in UV and optical were measured independently. The first step was to estimate a crude flux normalization amplitude for a 2000 km s^{-1} template at wavelengths where iron emission is strongest (see Table 2). Next the FWHM of the template was estimated, and then a fit of both the amplitude and FWHM was made. This was followed by another iteration of the continuum and the iron emission modeling.

The next step was to model the emission lines with multiple Gaussians (free parameters in the fit: height of the emission line peak, FWHM, and peak position). The inventory of emission lines and their components is presented in Table 3. In most cases strong emission lines such as Lyα C IV, C III], Mg II, and Hβ were modeled using two Gaussian components (a very broad line region component (VBLR) and the intermediate line region (ILR) component (see, e.g., Brotherton et al. 1994) which here we call the broad and narrow components, respectively. However, in a small number of cases (where the S/N was small or two components were clearly an excess) these lines were modeled using a single Gaussian. Due to the better quality of FOS spectra compared to the LBQS, additional line components representing blended lines were added: C III] λ1909 (modeled as C III] narrow + C III] broad + Si III] λ1892 + Al III λ1859 in higher S/N spectra, and as C III] single + Al III in lower S/N spectra), Hδ (Hδ + [S II] λ4072), and Hγ (Hγ + [O III] λ4363).

The continuum, iron, and emission line model obtained this way was then used as an input "continuum" to the FINDSL (Aldcroft 1993) routine, which identifies narrow absorption features and fits them with Gaussian profiles.

TABLE 3
INVENTORY OF EMISSION LINES

Emission Line	λ_c (Å)	FWHM[a] (km s^{-1})	Window[b] (Å)	Notes
Lyβ λ1025.7 + O VI λ1035.....	1030.0	5000	1010–1060	See Appendix.
Lyα λ1215.7.....	1215.7	7000s	1170–1350	
		2500n, 8000b	1170–1350	
N V λ1241.5.....	1241.5	6000	1170–1350	
O I λ1305.....	1305.0	2500	1170–1350	
Si IV + O IV] λ1400	1400.0	5800	1350–1450	
C IV λ1549.....	1549.0	6500s	1350–1720	
		3000n, 11000b	1350–1720	
He II λ1640.....	1640.0	10000	1350–1720	See Appendix.
Al III λ1859.....	1859.0	3500	1820–1970	
Si III] λ1892	1892.0	4000	1820–1970	
C III] λ1909.....	1909.0	5500s	1820–1970	
		1500n, 6000b	1820–1970	
Mg II λ2800.....	2800.0	4000s	2700–2900	Iron emission may be strong in this window.
		3000n, 8000b	2700–2900	Iron emission may be strong in this window.
[Ne V] λ3426.....	3426.0	1000	3390–3460	See Appendix.
[O II] λ3728.....	3728.0	600	3700–3760	See Appendix.
[Ne III] λ3869.....	3869.0	900	3810–3930	See Appendix.
Hδ λ4101.7.....	4101.7	450	4000–4200	
[S II] λ4072.5.....	4072.5	450	4000–4200	
Hγ λ4340.5	4340.5	3000	4240–4440	
[O III] λ4363.....	4263.0	1000	4240–4440	
He II λ4686.5.....	4686.5	1200	4580–4790	Iron emission may be strong in these windows.
Hβ λ4861.3	4861.3	4000s	4750–5100	Iron emission may be strong in these windows.
		1000n, 5500b	4750–5100	Iron emission may be strong in these windows.
[O III] λ4959.....	4959.0	700	4750–5100	Iron emission may be strong in these windows.
[O III] λ5007.....	5007.0	600	4750–5100	Iron emission may be strong in these windows.
He I λ5875.6.....	5875.6	2000	5825–5900	
[N II] λ6548	6548.1	700	6300–6800	
Hα λ6563.....	6562.8	1000n, 6000b	6300–6800	
[N II] λ6583	6583.4	700	6300–6800	
[S II] λ6716.4.....	6716.4	700	6300–6800	
[S II] λ6731	6730.8	700	6300–6800	

[a] This is the FWHM used for estimating the upper limits of W_λ in weak emission lines. More than one width is given for emission lines that can have two Gaussian components; s, single component; n, narrow component; b, broad component.

[b] The wavelength range over which the emission lines are modeled.

We excluded from the analysis the Lyα forest region blueward of $\lambda_{\rm rest} = 1065$ Å and also the Balmer continuum region (3360–3960 Å), where the global power-law continuum may not fit the spectra well. The minimum significance level for identification of absorption lines was set to 4.5 σ. The absorption line parameters were then used in a next iterative modeling step where the emission lines and the absorption lines were fitted simultaneously by the Sherpa program.

After each of the above steps, the results of the modeling were inspected and adjustments were made to those spectra that were not fitted successfully. This is not surprising as no automated procedure can be fully successful while dealing with the plethora of AGN spectral shapes.

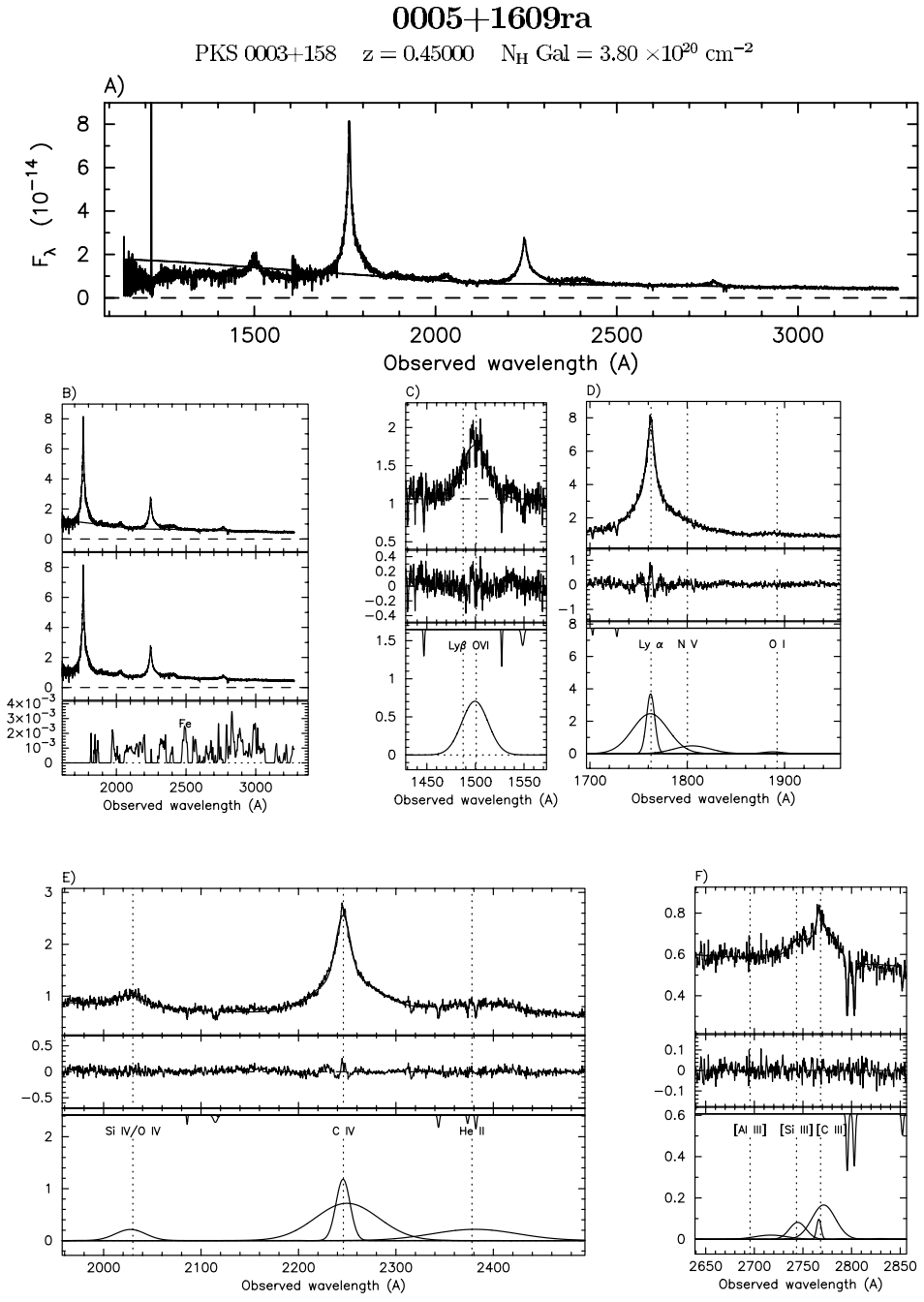

FIG. 1.—Example of spectral modeling for quasar PKS 0003+158. Panel (*a*) shows the reddened continuum model (fitted redward of Lyα) plotted over the observed spectrum. Panel (*b*) shows iron modeling and is divided into three frames: *top*, showing the continuum+iron model plotted over the overall spectrum; *middle*, showing the iron subtracted spectrum; and *bottom*, showing the fitted iron template. Panels (*c*) to (*f*) show modeling of the O VI, Lyα, C IV and C III] emission line regions. Each panel for each emission line region is divided into three frames, where the top frame shows the total best-fit model plotted over the relevant region of each spectrum, middle frame the residuals, and bottom frame the individual Gaussian components. (Note that Lyα, C IV and C III] are modeled with two components: narrow and broad, while other emission lines are modeled using one Gaussian.) The absorption lines that overlap each emission line are plotted at the top of the bottom panel. The dashed vertical lines in the emission line panels are drawn at the expected emission line position calculated using the redshift quoted at the top of the figure. Flux units are 10^{-14} ergs cm^{-2} s^{-1} Å^{-1}, wavelength units are in Å and are observed frame values. [*See the electronic edition of the Supplement for a color version of this figure.*]

The error analysis follows the procedure from Paper I (for details see § 3.5 of that paper), in which the 2 σ errors for each emission line parameter were determined from χ^2 confidence interval bounds ($\Delta\chi^2 = 4.0$). We determine upper limits for the amplitude of the line from the 2 σ positive error, estimated while fixing the line position at the expected wavelength and the FWHM at the median value found for that line in the LBQS sample (see Table 3).

Because of the large number of spectra in the pre-COSTAR FOS Spectral Atlas plots of spectral fits are available only in electronic form from our Web site.[1] In Figure 1 we present an example of one spectrum 0005+1609ra (PKS 0003+158) and its continuum, iron, emission, and absorption line modeling.

5. CONTINUUM AND EMISSION LINE MEASUREMENTS

The parameters of the power-law continuum are presented in Table 4, where column (1) gives the name of the spectrum, and column (2) the slope of the UV power-law continuum $\Gamma_{\rm UV}$ (where $f_\lambda \propto \lambda^{-\Gamma_{\rm UV}}$). For spectra with only one continuum window present, a constant slope of $\Gamma = 1$ (with no errors) was adopted, since the mean of the continuum slopes for the spectra in the FOS sample with more than one window, was 1.16 ± 0.89. In column (3) the normalization of the power law in units of 10^{-14} ergs cm^{-2} s^{-1} Å^{-1} is listed for the observed wavelength $\lambda_{\rm norm}$ given in column (4). For spectra extending toward the optical, a second power law was introduced with a slope $\Gamma_{\rm opt}$ presented in column (5). The optical power law was normalized at $\lambda_{\rm rest} = 4220$ Å to have the same continuum flux as the UV power law. The slopes and normalizations of the optical/UV continuum parameters are quoted with 2 σ errors.

In Table 5 we present in detail the emission line measurements for each object/spectrum from the pre-COSTAR FOS Spectral Atlas. However, due to the large size of this table it is available only in the electronic edition of the Supplement. For readers' convenience we present here a printed version of Table 5 in a digestible format for one example spectrum, 0005+1609ra.

6. STATISTICS

The number of emission lines we measured in the pre-COSTAR FOS/*HST* sample is shown in Table 6. The total number of emission lines modeled adds up to 1710 among which 86 are upper limits. Most measured lines lie in the UV range, and only a small number (9) of spectra extend toward optical wavelengths. The means and medians of the rest frame equivalent widths and FWHM for each emission line and their standard deviations are presented in Table 6. These are calculated for the detections (cols. [4]–[6] and [10]–[12]), and when upper limits are present a nonparametric survival analysis technique was used and a Kaplan-Meier estimator applied to estimate the means and medians of emission line parameters (cols. [7]–[8]; for reference see Isobe, Feigelson, & Nelson 1986 and Lavalley, Isobe, & Feigelson 1992). The means and medians of equivalent width for Lyα, C IV, C III], Mg II, and Hβ lines were calculated separately for single, narrow and broad components, as well as

[1] See http://hea-www.harvard.edu/~pgreen/HRCULES.html.

TABLE 4

CONTINUUM PARAMETERS

Designation (1)	$\Gamma_{\rm UV}$[a] (2)	Norm.[b] (3)	$\lambda_{\rm norm}$ (4)	$\Gamma_{\rm opt}$[a] (5)
0005+1609ra	$1.71^{+0.02}_{-0.02}$	$1.284^{+0.009}_{-0.009}$	2120.6	...
0010+1058ra	$0.94^{+0.09}_{-0.05}$	$1.208^{+0.028}_{-0.041}$	1593.1	...
0027+2241ra	$0.77^{+0.33}_{-0.37}$	$0.219^{+0.004}_{-0.004}$	3099.0	...
0047+0319ra	$1.17^{+0.61}_{-0.04}$	$0.338^{+0.032}_{-0.001}$	2373.9	...
0053+1241ra	$0.75^{+0.03}_{-0.02}$	$1.920^{+0.011}_{-0.013}$	2302.6	...
0054+2525ra	$0.21^{+0.48}_{-0.45}$	$2.016^{+0.106}_{-0.105}$	1689.2	...
0103+0221ra	$-0.07^{+3.42}_{-5.47}$	$0.066^{+0.014}_{-0.014}$	2037.3	...
0113+2958ra	$0.86^{+0.82}_{-0.64}$	$0.004^{+0.001}_{-0.001}$	1993.4	...
0115−0127ra.....	$1.38^{+0.22}_{-0.22}$	$0.079^{+0.002}_{-0.002}$	3458.8	...
0118+0258ra	$2.51^{+0.43}_{-0.43}$	$0.051^{+0.002}_{-0.002}$	2445.3	...
0123−5848ra.....	$1.46^{+0.03}_{-0.01}$	$4.459^{+0.033}_{-0.046}$	1531.2	...
0125−0005ra.....	$1.00^{+0.07}_{-0.31}$	$0.221^{+0.008}_{-0.002}$	3027.4	...
0136+2057ra	$1.86^{+0.05}_{-0.05}$	$0.169^{+0.003}_{-0.003}$	2084.1	...
0242−0000ra.....	$1.56^{+0.03}_{-0.03}$	$0.477^{+0.006}_{-0.006}$	4235.6	$0.71^{+0.06}_{-0.06}$
0242−0000rb	$1.35^{+0.06}_{-0.06}$	$0.308^{+0.006}_{-0.006}$	4235.6	$0.23^{+0.12}_{-0.11}$
0256−0126ra.....	$1.56^{+0.20}_{-0.20}$	$0.301^{+0.005}_{-0.005}$	2748.0	...
0319+4130ra	$3.12^{+2.92}_{-3.96}$	$0.389^{+0.071}_{-0.071}$	1488.1	...
0323−4930ra.....	$0.01^{+0.18}_{-0.16}$	$0.027^{+0.002}_{-0.002}$	1566.3	...
0336−3607ra.....	$2.23^{+0.50}_{-0.48}$	$0.048^{+0.002}_{-0.002}$	3071.2	...
0351−1429ra.....	$2.43^{+0.03}_{-0.30}$	$1.223^{+0.019}_{-0.008}$	2363.7	...
0352−0711ra.....	$1.57^{+0.81}_{-0.77}$	$0.235^{+0.011}_{-0.011}$	2869.4	...
0357−4812ra.....	$1.80^{+0.26}_{-0.26}$	$0.255^{+0.004}_{-0.004}$	2932.3	...
0405−1308ra.....	$1.46^{+0.05}_{-0.03}$	$0.197^{+0.002}_{-0.003}$	2296.9	...
0407−1211ra.....	$2.02^{+0.06}_{-0.06}$	$2.062^{+0.010}_{-0.011}$	2299.8	...
0417−0553ra.....	$1.62^{+0.16}_{-0.15}$	$0.491^{+0.008}_{-0.008}$	2595.9	...
0420−5456ra.....	$0.36^{+0.02}_{-0.03}$	$0.145^{+0.002}_{-0.002}$	4240.7	$1.16^{+0.07}_{-0.07}$
0441−4313ra.....	$1.54^{+0.12}_{-0.12}$	$0.271^{+0.003}_{-0.003}$	2329.8	...
0456−2159ra.....	$1.91^{+0.55}_{-0.02}$	$0.625^{+0.012}_{-0.001}$	2242.6	...
0506−6109ra.....	$1.05^{+0.87}_{-0.87}$	$0.094^{+0.005}_{-0.005}$	3061.0	...
0615+7102ra	$0.00^{+0.05}_{-0.74}$	$0.023^{+0.001}_{-0.001}$	4277.0	$-1.21^{+0.11}_{-0.10}$
0630+6905ra	1	$2.627^{+0.072}_{-0.072}$	1568.7	...
0630+6905rb	$1.49^{+0.11}_{-0.09}$	$0.163^{+0.005}_{-0.006}$	2003.6	...
0635−7516ra.....	$2.57^{+0.24}_{-0.24}$	$0.960^{+0.019}_{-0.019}$	2417.5	...
0713+1146ra	$1.15^{+0.13}_{-0.01}$	$0.385^{+0.018}_{-0.002}$	2588.6	...
0743−6726ra.....	1	$0.489^{+0.009}_{-0.009}$	3206.5	...
0744+3753ra	$1.49^{+0.07}_{-0.05}$	$0.079^{+0.001}_{-0.002}$	3017.1	...
0745+3142ra	$1.05^{+0.04}_{-0.03}$	$0.565^{+0.005}_{-0.005}$	2136.7	...
0755+2542ra	$-1.30^{+2.47}_{-3.27}$	$0.018^{+0.002}_{-0.002}$	2114.8	...
0837+4450ra	$-0.90^{+3.94}_{-2.62}$	$0.003^{+0.001}_{-0.001}$	1766.0	...
0840+1312ra	$0.96^{+0.05}_{-0.04}$	$0.090^{+0.001}_{-0.001}$	2458.2	...
0847+3445ra	$1.12^{+0.04}_{-0.03}$	$2.757^{+0.050}_{-0.059}$	1556.1	...
0853+4349ra	$1.83^{+0.17}_{-0.10}$	$0.301^{+0.003}_{-0.010}$	2214.1	...
0859+4637ra	1	$0.319^{+0.029}_{-0.029}$	2457.9	...
0902−1415ra.....	1	$0.207^{+0.012}_{-0.012}$	3083.3	...
0906+1646ra	$1.31^{+0.03}_{-0.03}$	$0.093^{+0.001}_{-0.001}$	2065.2	...
0909+4253ra	$0.25^{+0.30}_{-0.29}$	$0.027^{+0.001}_{-0.001}$	2442.4	...
0919+5106ra	$1.42^{+0.14}_{-0.14}$	$0.510^{+0.006}_{-0.006}$	2276.1	...
0927+3902ra	$1.86^{+0.03}_{-0.02}$	$0.414^{+0.002}_{-0.003}$	2478.6	...
0927+3902rb	$1.80^{+0.04}_{-0.03}$	$0.213^{+0.002}_{-0.002}$	2478.6	...
0955+6903ra	$-1.86^{+6.34}_{-84.78}$	$0.117^{+0.053}_{-0.055}$	1462.4	...
0955+6903rb	$0.28^{+0.39}_{-0.43}$	$0.174^{+0.012}_{-0.012}$	4219.6	...
0955+6903rc.....	$-0.60^{+0.25}_{-0.23}$	$0.133^{+0.010}_{-0.010}$	2238.1	...
0956+4115ra	$1.72^{+0.03}_{-0.02}$	$1.460^{+0.012}_{-0.014}$	1804.9	...
0957+5522ra	$1.00^{+0.18}_{-0.18}$	$0.062^{+0.001}_{-0.001}$	2791.9	...
0958+3224ra	$1.52^{+0.20}_{-0.19}$	$0.355^{+0.004}_{-0.004}$	2238.4	...
1003+6813ra	$0.38^{+0.14}_{-0.15}$	$0.354^{+0.006}_{-0.006}$	2593.0	...
1004+2855ra	$1.74^{+0.03}_{-0.02}$	$1.324^{+0.009}_{-0.009}$	1944.7	...
1010+4132ra	$1.96^{+0.04}_{-0.04}$	$0.542^{+0.005}_{-0.005}$	2358.0	...
1011+1304ra	1	$0.356^{+0.006}_{-0.006}$	3030.3	...
1013+3551ra	$1.50^{+1.62}_{-1.81}$	$1.084^{+0.108}_{-0.108}$	1564.9	...
1024+1912ra	1	$0.128^{+0.007}_{-0.007}$	2422.1	...
1041+0610ra	1	$0.409^{+0.036}_{-0.036}$	2503.4	...
1042+1203ra	1	$0.119^{+0.008}_{-0.008}$	2323.2	...

TABLE 4—*Continued*

Designation (1)	Γ_{UV}[a] (2)	Norm.[b] (3)	λ_{norm} (4)	Γ_{opt}[a] (5)
1048−2509ra.....	$0.00^{+0.10}_{-0.14}$	$0.027^{+0.002}_{-0.002}$	4270.6	$-1.90^{+0.22}_{-0.06}$
1051−0051ra.....	$1.62^{+0.04}_{-0.03}$	$0.866^{+0.007}_{-0.009}$	1988.9	...
1058+1951ra	1	$0.243^{+0.011}_{-0.011}$	2416.0	...
1104+7658ra	$1.28^{+0.03}_{-0.02}$	$1.087^{+0.006}_{-0.009}$	1918.1	...
1106−0052ra.....	$1.43^{+0.07}_{-0.05}$	$0.418^{+0.007}_{-0.009}$	2081.6	...
1107+1628ra	$1.83^{+0.08}_{-0.08}$	$0.657^{+0.008}_{-0.008}$	2386.8	...
1114+4037ra	$1.66^{+0.06}_{-0.04}$	$0.076^{+0.001}_{-0.001}$	2536.0	...
1119+2119ra	$1.61^{+0.02}_{-0.02}$	$4.088^{+0.023}_{-0.027}$	1720.6	...
1125+5910ra	1	$0.358^{+0.017}_{-0.017}$	2461.9	...
1130−1449ra.....	$0.53^{+0.75}_{-0.82}$	$0.130^{+0.006}_{-0.006}$	3198.5	...
1132+1023ra	$1.12^{+0.30}_{-0.01}$	$0.315^{+0.001}_{-0.032}$	2199.6	...
1139+6547ra	$1.81^{+0.05}_{-0.04}$	$0.547^{+0.007}_{-0.009}$	2407.3	...
1139−1350ra.....	$1.59^{+0.17}_{-0.16}$	$0.457^{+0.006}_{-0.006}$	2281.5	...
1139−3744ra.....	$1.11^{+0.02}_{-0.01}$	$22.191^{+0.086}_{-0.152}$	1474.9	...
1151+5437ra	$1.27^{+0.26}_{-0.25}$	$0.444^{+0.007}_{-0.007}$	2879.7	...
1158+6254ra	$1.33^{+0.38}_{-0.36}$	$0.362^{+0.014}_{-0.014}$	2331.2	...
1204+2754ra	$0.49^{+0.05}_{-0.06}$	$0.221^{+0.004}_{-0.005}$	1704.3	...
1208+4540ra	$1.00^{+1.49}_{-0.04}$	$0.425^{+0.006}_{-0.006}$	3156.1	...
1210+0954rA	$1.00^{+1.60}_{-1.45}$	$0.017^{+0.002}_{-0.002}$	7045.3	...
1210+0954rB.....	$1.00^{+2.75}_{-0.80}$	$0.005^{+0.001}_{-0.001}$	7045.3	...
1210+3924ra*.....	$1.70^{+0.01}_{-0.01}$	$8.390^{+0.008}_{-0.008}$	4233.9	$1.6^{+0.04}_{-0.03}$
1210+3924rb	$1.05^{+0.44}_{-0.45}$	$33.921^{+0.695}_{-0.696}$	1467.3	...
1210+3924rc.....	$0.89^{+0.48}_{-0.51}$	$9.335^{+0.213}_{-0.212}$	1467.3	...
1214+1403ra	$1.12^{+0.01}_{-0.01}$	$0.874^{+0.006}_{-0.007}$	4561.4	$2.69^{+0.11}_{-0.11}$
1219+0638ra	$1.56^{+0.03}_{-0.02}$	$1.077^{+0.006}_{-0.008}$	1947.0	...
1221+7518ra	$2.04^{+1.06}_{-0.97}$	$2.023^{+0.126}_{-0.126}$	1566.0	...
1221+7518rb	$1.52^{+0.02}_{-0.01}$	$2.493^{+0.012}_{-0.020}$	1815.0	...
1225+3332ra	$0.04^{+0.01}_{-0.01}$	$0.138^{+0.001}_{-0.001}$	1464.0	...
1229+0203ra	$1.72^{+0.02}_{-0.02}$	$24.331^{+0.135}_{-0.149}$	1694.0	...
1230+1223rA	$0.01^{+0.07}_{-0.07}$	$0.109^{+0.002}_{-0.002}$	4237.7	$0.46^{+0.10}_{-0.09}$
1230+1223rB.....	$0.00^{+0.18}_{-0.90}$	$0.007^{+0.001}_{-0.001}$	4237.7	$-2.25^{+0.26}_{-0.24}$
1231−0224ra.....	1	$0.210^{+0.025}_{-0.025}$	2341.5	...
1233+0931ra	$-0.25^{+0.96}_{-1.06}$	$0.577^{+0.029}_{-0.029}$	2069.4	...
1244+1721ra	1	$0.406^{+0.006}_{-0.006}$	3011.7	...
1247+3209ra	1	$0.150^{+0.012}_{-0.012}$	2489.8	...
1252+5634ra	$1.44^{+0.02}_{-0.02}$	$0.171^{+0.002}_{-0.002}$	1932.0	...
1254+1141ra	$1.32^{+0.16}_{-0.15}$	$0.217^{+0.003}_{-0.003}$	2736.3	...
1256−0547ra.....	$0.31^{+0.02}_{-0.02}$	$0.267^{+0.003}_{-0.004}$	2246.7	...
1259+3423ra	1	$0.092^{+0.002}_{-0.002}$	3146.9	...
1301+5902ra	$1.55^{+0.11}_{-0.01}$	$1.005^{+0.002}_{-0.029}$	2138.5	...
1305−1033ra.....	$1.43^{+0.02}_{-0.02}$	$3.001^{+0.018}_{-0.019}$	1869.7	...
1305−1033rb	1	$0.109^{+0.022}_{-0.022}$	1463.8	...
1308+3005ra	$1.70^{+0.19}_{-0.19}$	$0.245^{+0.004}_{-0.004}$	2641.3	...
1309+0819ra	$0.30^{+0.53}_{-0.55}$	$1.135^{+0.069}_{-0.069}$	1689.2	...
1319+2728ra	$1.76^{+0.19}_{-0.20}$	$0.510^{+0.006}_{-0.006}$	2957.2	...
1319+5148ra	$1.74^{+0.26}_{-0.26}$	$0.217^{+0.004}_{-0.004}$	3012.8	...
1323+2910ra	1	$0.142^{+0.036}_{-0.036}$	2503.4	...
1331+3030ra	1	$0.178^{+0.028}_{-0.028}$	2362.1	...
1336+1725ra	$1.23^{+0.16}_{-0.16}$	$0.507^{+0.006}_{-0.006}$	2271.7	...
1341+4123ra	$1.73^{+0.26}_{-0.24}$	$0.250^{+0.004}_{-0.004}$	3245.3	...
1342+6021ra	$0.86^{+0.33}_{-0.35}$	$0.082^{+0.002}_{-0.002}$	2868.0	...
1343+2844ra	1	$0.199^{+0.013}_{-0.013}$	2433.6	...
1349+5341ra	1	$0.101^{+0.007}_{-0.007}$	2267.1	...
1354+0052ra	$1.14^{+0.34}_{-0.35}$	$0.337^{+0.006}_{-0.006}$	3096.1	...
1357+1919ra	$1.46^{+0.07}_{-0.06}$	$0.333^{+0.006}_{-0.007}$	2515.5	...
1358+5752ra	1	$0.166^{+0.009}_{-0.009}$	3141.6	...
1359−4152ra.....	$0.30^{+0.32}_{-0.30}$	$1.689^{+0.057}_{-0.057}$	1920.3	...
1404+0937ra	$-4.63^{+2.37}_{-3.09}$	$0.162^{+0.016}_{-0.016}$	2107.5	...
1405+2555ra	$0.69^{+0.38}_{-0.42}$	$1.556^{+0.070}_{-0.070}$	1702.4	...
1409+2618ra	$2.16^{+0.20}_{-0.20}$	$0.506^{+0.007}_{-0.007}$	2837.2	...

TABLE 4—*Continued*

Designation (1)	Γ_{UV}[a] (2)	Norm.[b] (3)	λ_{norm} (4)	Γ_{opt}[a] (5)
1417+2508ra	$0.58^{+0.04}_{-0.01}$	$0.898^{+0.007}_{-0.017}$	1487.5	...
1417+2508rb	$1.04^{+0.11}_{-0.09}$	$3.797^{+0.135}_{-0.148}$	1487.5	...
1417+4456ra	$1.00^{+1.01}_{-0.34}$	$0.459^{+0.006}_{-0.006}$	2417.4	...
1418+1703ra	1	$0.102^{+0.007}_{-0.007}$	2412.8	...
1427+1949ra	$1.00^{+0.22}_{-1.02}$	$1.756^{+0.112}_{-0.111}$	1627.8	...
1427−1203ra.....	$2.27^{+0.19}_{-0.19}$	$0.327^{+0.006}_{-0.006}$	2641.3	...
1436+6336ra	1	$0.194^{+0.007}_{-0.007}$	3271.7	...
1437−0147ra.....	1	$0.710^{+0.076}_{-0.076}$	2503.4	...
1442+3526ra	1	$2.106^{+0.118}_{-0.118}$	1828.9	...
1445+0958ra	1	$1.536^{+0.009}_{-0.011}$	1853.4	...
1454−3747ra.....	$0.12^{+0.27}_{-0.26}$	$0.377^{+0.011}_{-0.011}$	1921.7	...
1514+3650ra	$2.08^{+0.04}_{-0.03}$	$0.716^{+0.005}_{-0.008}$	2004.6	...
1524+0958ra	1	$0.514^{+0.005}_{-0.005}$	3075.3	...
1539+4735ra	1	$0.635^{+0.012}_{-0.012}$	2263.9	...
1539+4735rb	$1.35^{+0.10}_{-0.10}$	$0.588^{+0.006}_{-0.006}$	2591.7	...
1547+2052ra	$1.37^{+0.03}_{-0.03}$	$0.769^{+0.011}_{-0.011}$	1849.0	...
1557+3304ra	$1.06^{+0.46}_{-0.47}$	$0.028^{+0.001}_{-0.001}$	2840.2	...
1613+3412ra	$1.31^{+0.20}_{-0.20}$	$0.081^{+0.001}_{-0.001}$	3511.5	...
1614+2604ra	1	$0.686^{+0.069}_{-0.069}$	1654.1	...
1620+1736ra	$1.62^{+0.14}_{-0.13}$	$0.572^{+0.007}_{-0.007}$	2274.3	...
1620+1736rb	$1.70^{+0.04}_{-0.03}$	$0.446^{+0.004}_{-0.006}$	2274.3	...
1633+3924ra	$2.43^{+0.68}_{-0.75}$	$0.110^{+0.005}_{-0.005}$	2958.6	...
1634+7031ra	1	$1.945^{+0.013}_{-0.013}$	3092.6	...
1638+5720ra	$1.87^{+0.05}_{-0.04}$	$0.279^{+0.003}_{-0.004}$	2560.3	...
1642+3948ra	$0.91^{+0.06}_{-0.06}$	$0.324^{+0.005}_{-0.006}$	2329.5	...
1658+0515ra	1	$0.209^{+0.015}_{-0.015}$	2489.7	...
1704+6044ra	$1.50^{+0.03}_{-0.03}$	$1.087^{+0.010}_{-0.012}$	2006.7	...
1719+4804ra	$1.58^{+0.12}_{-0.12}$	$1.338^{+0.010}_{-0.010}$	3047.9	...
1821+6420ra	$1.52^{+0.01}_{-0.01}$	$5.336^{+0.016}_{-0.024}$	1896.9	...
1927+7358ra	$1.24^{+0.03}_{-0.02}$	$1.017^{+0.008}_{-0.011}$	1904.3	...
2044−1043ra.....	$1.15^{+0.01}_{-0.01}$	$11.316^{+0.031}_{-0.049}$	1512.8	...
2114+0607ra	$0.82^{+0.05}_{-0.03}$	$0.569^{+0.003}_{-0.010}$	2144.0	...
2131−1207ra.....	$1.56^{+0.03}_{-0.03}$	$1.156^{+0.008}_{-0.008}$	2195.2	...
2137−1432ra.....	$-0.40^{+0.19}_{-0.22}$	$0.599^{+0.014}_{-0.014}$	1755.4	...
2143+1743ra	$1.01^{+0.03}_{-0.03}$	$1.097^{+0.013}_{-0.014}$	1771.2	...
2148+0657ra	$1.78^{+0.30}_{-0.29}$	$0.360^{+0.007}_{-0.007}$	2910.4	...
2203+3145ra	$1.43^{+0.02}_{-0.02}$	$2.133^{+0.018}_{-0.020}$	1893.9	...
2218−0335ra.....	$1.01^{+0.06}_{-0.05}$	$0.224^{+0.003}_{-0.004}$	2780.2	...
2218−0335rc.....	$1.29^{+0.06}_{-0.06}$	$0.206^{+0.003}_{-0.003}$	2780.2	...
2225−0457ra.....	$0.41^{+0.34}_{-0.34}$	$0.037^{+0.001}_{-0.001}$	3515.9	...
2232+1143ra	$1.37^{+0.04}_{-0.04}$	$0.198^{+0.002}_{-0.002}$	2979.1	...
2246−1206ra.....	$2.30^{+0.12}_{-0.12}$	$0.581^{+0.008}_{-0.008}$	2383.9	...
2253+1608ra	$1.10^{+0.16}_{-0.15}$	$0.476^{+0.007}_{-0.007}$	2718.8	...
2253+1608rb	$1.06^{+0.04}_{-0.03}$	$0.286^{+0.003}_{-0.003}$	2718.8	...
2254+1136ra	$0.82^{+0.03}_{-0.02}$	$0.739^{+0.011}_{-0.012}$	1938.5	...
2303−6807ra.....	$1.48^{+0.13}_{-0.12}$	$0.236^{+0.005}_{-0.005}$	2211.3	...
2311+1008ra	$1.63^{+0.03}_{-0.03}$	$0.683^{+0.006}_{-0.006}$	2096.2	...
2342−0322ra.....	$1.57^{+0.14}_{-0.14}$	$0.467^{+0.006}_{-0.006}$	2772.9	...
2346+0930ra	$1.20^{+0.16}_{-0.15}$	$0.429^{+0.007}_{-0.007}$	2452.6	...
2351−0109ra.....	$1.79^{+1.12}_{-0.96}$	$0.410^{+0.046}_{-0.046}$	1717.0	...
2355−3357ra.....	$1.59^{+0.12}_{-0.12}$	$0.355^{+0.004}_{-0.004}$	2495.0	...

NOTES.—Table 4 is also available in machine-readable form in the electronic edition of the *Astrophysical Journal Supplement*. (*) See notes on individual spectra in the Appendix.

[a] The power-law continuum slopes Γ_{UV} and Γ_{opt} are defined as $f_\lambda \propto \lambda^{-\Gamma}$. Γ_{UV} is fitted at $\lambda_{rest} < 4200$, Γ_{opt} at $\lambda_{rest} > 4200$. Slopes with no listed errors show the assumed slope value in cases where only a single continuum window was available.

[b] Normalization of the UV power law in units of 10^{-14} ergs cm^{-2} s^{-1} Å^{-1}, at observed wavelength λ_{norm}.

TABLE 5

REPRESENTATIVE EMISSION LINE MEASUREMENTS

Emission Line (1)	FWHM (km s^{-1}) (2)	$\Delta v_{\rm peak}$ (km s^{-1}) (3)	W_λ (Å) (4)	Observed Flux (10^{-14} ergs cm^{-2} s^{-1}) (5)	Absorption Lines (6)
Designation: 0005+1609ra, Redshift: $z = 0.45000$					
UV iron	1000^{+9000}_{-250}	...	$2.6^{+3.7}_{-2.5}$	$2.4^{+3.4}_{-2.3}$	...
Optical iron	...	...	...	...	...
Lyβ	6400^{+220}_{-200}	1200^{+100}_{-100}	$15.5^{+1.0}_{-1.0}$	$23.9^{+1.6}_{-1.5}$	3
Lyα narrow	1680^{+40}_{-40}	-60^{+20}_{-20}	$24.1^{+1.2}_{-1.1}$	$61.6^{+3.0}_{-2.9}$	...
Lyα broad	7350^{+80}_{-80}	-120^{+40}_{-40}	$70.7^{+1.6}_{-1.5}$	$180.4^{+4.1}_{-3.9}$	2
N v	7000^{+3600}_{-80}	800^{+320}_{-90}	$14.6^{+8.1}_{-0.7}$	$36.0^{+20.0}_{-1.7}$	...
O i	3600^{+1200}_{-600}	-700^{+380}_{-380}	$1.9^{+1.0}_{-0.6}$	$4.4^{+2.4}_{-1.3}$	...
Si iv + O iv]	5400^{+320}_{-320}	-350^{+160}_{-160}	$7.1^{+0.8}_{-0.8}$	$14.3^{+1.7}_{-1.6}$	3
C iv narrow	2260^{+30}_{-30}	-50^{+10}_{-10}	$22.3^{+0.5}_{-0.5}$	$37.56^{+0.9}_{-0.9}$	...
C iv broad	10200^{+90}_{-80}	420^{+40}_{-40}	$61.2^{+0.9}_{-1.0}$	$103.0^{+1.6}_{-1.6}$	...
He ii blend	13000^{+400}_{-400}	300^{+240}_{-240}	$25.3^{+1.7}_{-1.6}$	$38.7^{+2.6}_{-2.4}$	3
Al iii	4500^{+2800}_{-2100}	2500^{+1200}_{-1000}	$1.0^{+1.3}_{-0.7}$	$1.2^{+1.6}_{-0.9}$	...
Si iii]	2200^{+420}_{-380}	100^{+200}_{-200}	$2.1^{+0.7}_{-0.6}$	$2.6^{+0.9}_{-0.8}$	...
C iii] narrow	500^{+220}_{-200}	-200^{+90}_{-90}	$0.7^{+0.5}_{-0.3}$	$0.8^{+0.6}_{-0.4}$	...
C iii] broad	3100^{+220}_{-200}	350^{+120}_{-120}	$6.2^{+0.8}_{-0.8}$	$7.3^{+1.0}_{-0.9}$	3

NOTES.—Table 5 is available in its entirety in the electronic edition of the *Astrophysical Journal Supplement*. A portion is shown here for guidance regarding its form and content. We present here line measurements for one example spectrum 0005+1609ra. All measurements are rest frame except for flux. $\Delta v_{\rm peak}$ is the offset of the peak of the Gaussian emission line model, in km s^{-1}, from the expected position based on the tabulated redshift. Spectral modeling of this object is shown in Fig. 1.

TABLE 6

REST FRAME EMISSION LINE PARAMETER DISTRIBUTIONS

			W_λ (Å)						FWHM (km s^{-1})		
			Detected			Kaplan-Meier			Detected		
EMISSION LINE (1)	TOTAL (2)	LIMITS (3)	Mean (4)	SD (5)	Median (6)	Mean (7)	Median (8)	NUM. (9)	Mean (10)	SD (11)	Median (12)
UV iron	85	22	47 ± 7	55	43.6	35.7 ± 3.6	35.5	64	4960 ± 730	5880	4500
Optical iron	9	1	85 ± 25	70	58.5	76.0 ± 28.4	46.7	9	8080 ± 3130	9380	10000
Lyβ + O vi	97	2	12 ± 2	15	11.8	12.2 ± 0.8	11.4	95	6130 ± 690	6720	5500
Lyα:											
Single[a]	10	0	229 ± 156	493	64.5	...	...	10	6220 ± 2540	8040	6100
Narrow	133	0	29 ± 3	38	23.8	...	...	133	2380 ± 220	2560	2260
Broad	133	0	74 ± 8	93	62.5	...	...	133	10050 ± 960	11080	8900
Sum[b]	143	0	112 ± 15	175	87.2	...	...	...	...	...	...
N v	141	12	15 ± 2	19	12.5	13.5 ± 1.1	11.4	133	5430 ± 540	6220	5800
O i	133	17	2.9 ± 0.4	4	2.2	4.8 ± 2.2	1.9	122	2930 ± 300	3270	3200
Si iv + O iv]	129	0	13 ± 2	25	8.0	...	...	129	6360 ± 650	7400	5600
C iv:											
Single[a]	4	0	21 ± 16	32	20.6	...	...	4	4430 ± 3070	6140	3950
Narrow	121	0	30 ± 4	46	21.1	...	...	121	2900 ± 290	3140	2650
Broad	121	0	63 ± 7	79	49.5	...	...	121	11090 ± 1070	11790	10400
Sum[b]	125	0	91 ± 11	118	68.8	...	...	...	...	...	...
He ii λ1640	110	2	20 ± 3	26	16.9	19.7 ± 1.5	16.7	109	10890 ± 1110	11560	11500
Al iii	91	17	6 ± 1	11	3.6	5.0 ± 1.0	2.5	75	5550 ± 770	6660	5400
C iii]:											
Single[a]	45	0	21 ± 5	32	13.9	...	...	45	4890 ± 780	5260	4800
Narrow	47	0	7 ± 13	10	4.0	...	...	47	1730 ± 310	2140	1400
Broad	47	0	20 ± 4	24	18.0	...	...	47	8270 ± 1660	11370	5700
Sum[b]	92	0	24 ± 3	32	17.9	...	...	...	...	...	...
Si iii]	45	7	3 ± 1	5	1.9	2.8 ± 0.6	1.5	38	2780 ± 600	3680	2000
Mg ii:											
Single[a]	8	2	136 ± 92	227	62.1	101.9 ± 53.0	50.5	6	3840 ± 1850	4530	3620
Narrow	25	0	29 ± 9	44	18.0	...	...	26	3260 ± 760	3880	2600
Broad	25	0	33 ± 8	41	27.9	...	...	26	8230 ± 1850	9430	8400
Sum[b]	33	2	76 ± 21	115	50.5	71.5 ± 14.6	49.4	...	...	...	...

TABLE 6—*Continued*

			W_λ (Å)						FWHM (km s^{-1})		
			Detected			Kaplan-Meier			Detected		
Emission Line (1)	Total (2)	Limits (3)	Mean (4)	SD (5)	Median (6)	Mean (7)	Median (8)	Num. (9)	Mean (10)	SD (11)	Median (12)
[Ne v]	13	1	39 ± 20	69	4.5	35.9 ± 14.5	4.4	12	920 ± 370	1260	700
[O ii]	10	0	142 ± 92	291	24.7	...	...	10	1210 ± 460	1470	1210
[Ne iii]	9	0	98 ± 56	169	70.0	...	...	9	1500 ± 620	1860	1450
Hδ	8	0	32 ± 18	51	26.9	...	...	9	2610 ± 1380	4130	1500
[S ii] λ4072.5	7	0	22 ± 13	35	10.1	...	...	8	1050 ± 440	1250	1080
Hγ	7	0	25 ± 14	38	9.9	...	...	8	1600 ± 980	2780	950
[O iii] λ4363	7	0	16 ± 8	21	15.8	...	...	8	1300 ± 520	1480	1300
He ii λ4686	8	0	31 ± 15	41	28.3	...	...	9	2870 ± 1380	4130	1550
Hβ:											
Single[a]	2	0	70 ± 96	135	70.4	...	...	2	6700 ± 8540	12080	6700
Narrow	5	0	46 ± 26	58	36.1	...	...	6	870 ± 420	1040	770
Broad	5	0	88 ± 59	132	35.5	...	...	6	8310 ± 5400	13230	4550
Sum[b]	7	0	116 ± 61	162	61.4	...	...	...	...	...	...
[O iii] λ4959	7	0	218 ± 134	354	208.20	...	...	8	1070 ± 460	1290	1140
[O iii] λ5007	7	0	629 ± 384	1018	611.2	...	...	8	1100 ± 460	1300	1280
He i	7	1	8 ± 4	11	5.9	7.7 ± 2.2	4.8	7	1530 ± 950	2500	900
[N ii] λ6548	6	0	25 ± 13	31	26.2	...	...	7	840 ± 380	1010	700
Hα:											
Single[a]	0	0	...	...	...	...	...	...	...	...	...
Narrow	6	0	68 ± 40	98	61.5	...	...	7	810 ± 370	990	800
Broad	6	0	325 ± 234	575	198.0	...	...	7	2700 ± 1280	3380	2150
Sum[b]	6	0	392 ± 258	633	308.5	...	...	...	...	...	...
[N ii] λ6583	6	0	67 ± 36	88	56.9	...	...	7	530 ± 230	620	500
[S ii] λ6716.4	5	0	20 ± 10	23	23.0	...	...	6	910 ± 480	1180	1030
[S ii] λ6731	5	0	6 ± 4	9	3.7	...	...	6	680 ± 430	1050	300

Notes.—Col. (1), Emission line or line blend; col. (2), total number of emission lines modeled; col. (3), number of upper limits; col. (4), mean W_λ of detected emission lines; col. (5), standard deviation (SD) of W_λ measurements for detected emission lines; col. (6), median of W_λ for detections, cols. (7)–(8), Kaplan-Meier reconstructed mean and median of W_λ distribution; cols. (9)–(12), the number, mean, and median of the distribution of FWHM of the Gaussian components used to model each emission feature.

[a] The distribution for single Gaussian component models are tabulated separately from narrow and broad components.

[b] The distribution of the sum of the broad and narrow component W_λ measurements included with the single component measurements.

for the whole line (called "sum" in Table 6) defined as the sum of narrow and broad components for the two Gaussian models and single component for the single Gaussian model.

The histograms of W_λ and FWHM for emission lines blueward of [Ne v] are presented in Figure 2. The first and third rows give the distributions for W_λ, while the second and fourth rows give the FWHM distributions. In all panels, solid lines represent distributions for detections, while the dotted lines show the estimated W_λ distributions from the Kaplan-Meier estimator (see, e.g., Fe UV). In the panels that show the sum of Lyα, C iv, C iii] and Mg ii distributions, the shaded histograms represent results from single Gaussian component fits.

7. DISCUSSION

Comparison of the FOS sample with the previously studied LBQS sample (Paper I) shows that the means and medians of the equivalent width of the strong emission lines (UV iron, Lyβ, Lyα, C iv, Mg ii, and He ii) are larger in the FOS sample than in the LBQS sample. The one-tailed Kolmogorov-Smirnov test showed that the values of the equivalent widths of the FOS sample were larger than the values of the equivalent widths of the LBQS sample at more than 95%, 99%, 99%, 99.9%, 99.9%, and 99.9% significance level for UV iron, Lyβ, Lyα, C iv, He ii, and Mg ii lines, respectively. This trend reflects the Baldwin effect (BEff), i.e., the known anticorrelation between the line equivalent width and luminosity found in AGNs. Since the FOS sample extends toward lower redshifts and luminosities than the LBQS (see Fig. 3 for $L_{\rm opt}$ vs. z dependence of the two samples), extension toward higher equivalent widths is also expected. The weaker lines or blends such as N v, O i, Si iv + O vi], C iii], and Al iii have mean and median values, similar to or smaller than the LBQS values. The one-tailed Kolmogorov-Smirnov test showed that the values of the equivalent widths of the FOS sample were smaller than the values of the equivalent widths of the LBQS sample at more than 99.9%, 95%, 99.9%, 99.9%, and 99.9% significance level for N v, O i, Si iv + O vi], C iii], and Al iii lines, respectively, which is inconsistent with the BEff for these lines. However, since N v and O i do not show a BEff (see § 7.1 below) and the C iii] + Al iii blend has been modeled including the Si iii] line in half of the FOS spectra (making the equivalent widths smaller) and none of the LBQS spectra, this is expected.

7.1. *The Baldwin Effect*

We now study the correlations between W_λ and UV luminosity, i.e., the Baldwin effect. We use the rest frame monochromatic luminosity at 2500 Å obtained from the B magnitude (assembled from the Veron-Cetty & Veron 1996

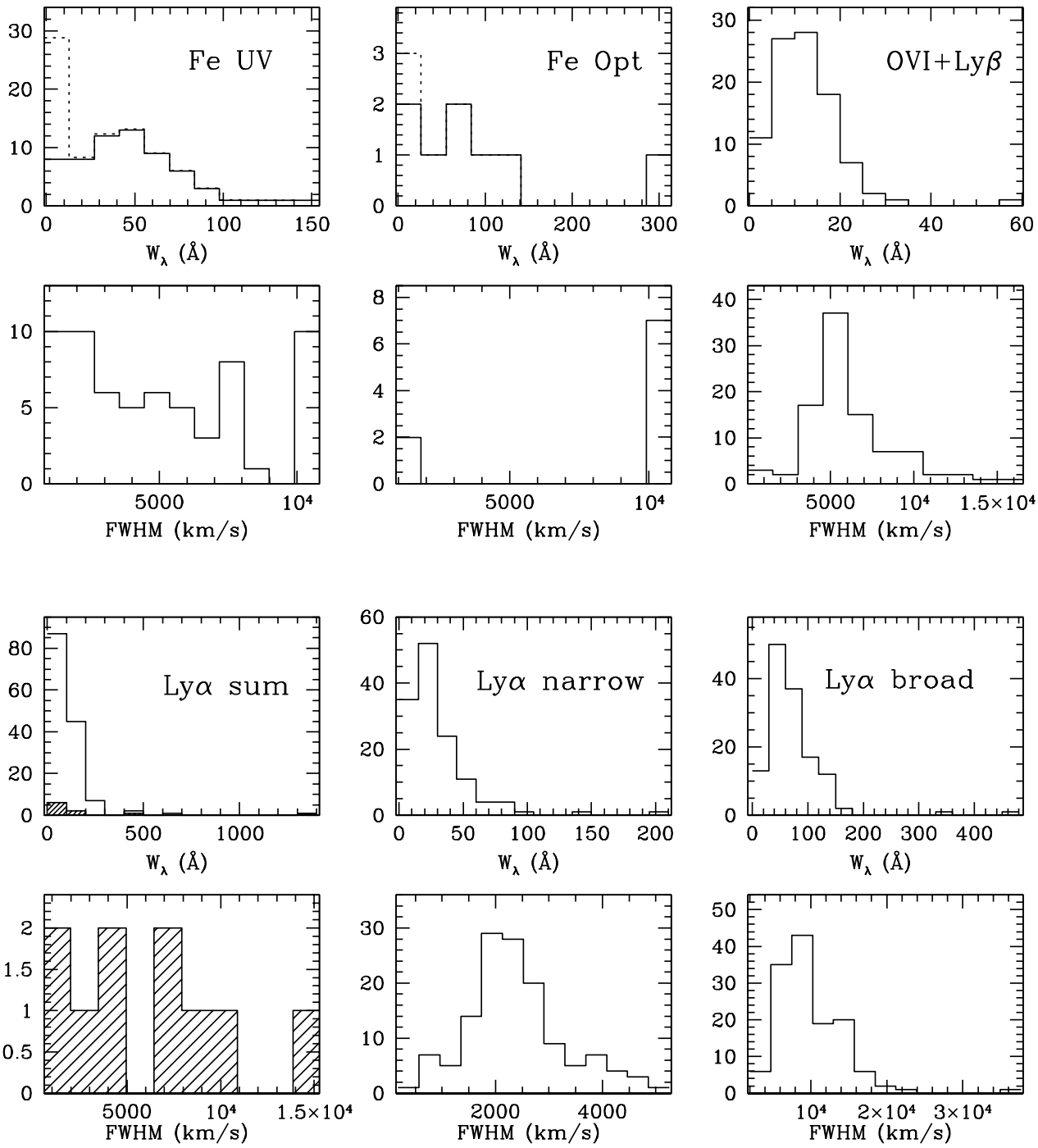

FIG. 2.—Distribution of rest frame W_λ (*top and third row*) and FWHM (*second from top and bottom row*) of the emission line properties of AGNs in the pre-COSTAR FOS sample. Dotted lines represent the estimated Kaplan-Meier distributions, shown for emission lines which have more than 10% of upper limits in their measurements. Shaded areas represent single Gaussian component distributions.

Catalog of quasars and AGNs), assuming a continuum slope $\alpha = 0.5$ (where $f_\nu \sim \nu^\alpha$) and $H_0 = 50$ km s^{-1} Mpc^{-1}, $q_0 = 0.5$, and $\Lambda = 0$. We use the survival analysis package ASURV (Lavalley et al. 1992) to allow for the presence of a small number of upper limits in our data and applied the following tests: the Cox proportional hazard model, the generalized Kendall rank and the Spearman rank test. We considered a correlation significant if the probability of the correlation occurring by chance was $\leq 1\%$ in all these tests. The probabilities, slopes, and intercept coefficients of the Baldwin effect regressions are quoted in Table 7. We found a significant Baldwin effect for the major emission lines: Lyα, Si IV, and C IV. These correlations have been found previously in the LBQS sample as well as by other authors (Kinney, Rivolo, & Koratkar 1990; Zamorani et al. 1992; Espey & Andreadis 1999). We confirm the Lyβ BEff discovered by Zheng, Kriss, & Davidsen (1995). This was not significant in the LBQS data (unless only the detections were analyzed), probably due to an insufficient luminosity range (1 dex in LBQS cf. 2.5 dex in FOS).

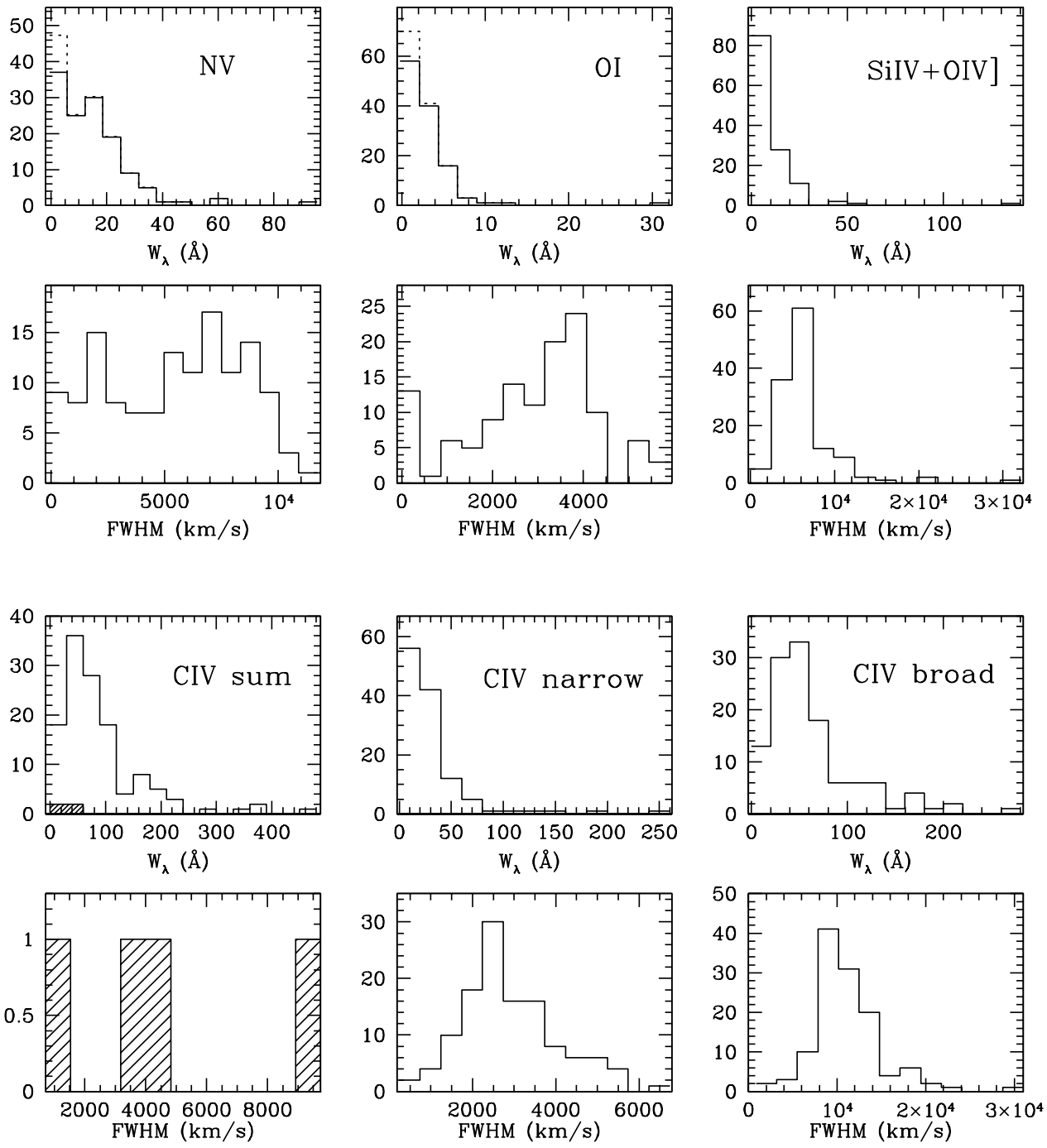

FIG. 2.—*Continued*

We find a weak Baldwin effect in Fe UV when all data are analyzed ($P = 0.03/0.05/0.05$ in Cox/Kendall/Spearman test) and a marginally significant correlation when only the detections are analyzed ($P = 0.02/0.00/0.00$). When the FOS and LBQS data are combined together the Baldwin effect is significant with the probability of a chance correlation less than 0.01%, confirming the BEff discovered in Paper I. The optical iron will not be studied here since the number of new points (10) is too small to conduct any reasonable statistical analysis.

We also find a significant BEff for C III] which was not detected in the LBQS. This could be due either to a larger L(2500 Å) range covered by the FOS sample or to a more detailed model fit of the C III] region here which includes the Si III] emission feature. We also find a Si III] BEff which has not been previously reported.

No BEff is present for N V. This line is sensitive to the abundances (Hamann & Ferland 1993), and the abundances are claimed to increase with redshift or luminosity, working against the BEff (Ferland et al. 1996; Dietrich & Wilhelm-Erkens 2000). No BEff was found for O I (either here or in the LBQS) or for Al III (present in LBQS). Mg II does not show any BEff perhaps due to too few data points (33).

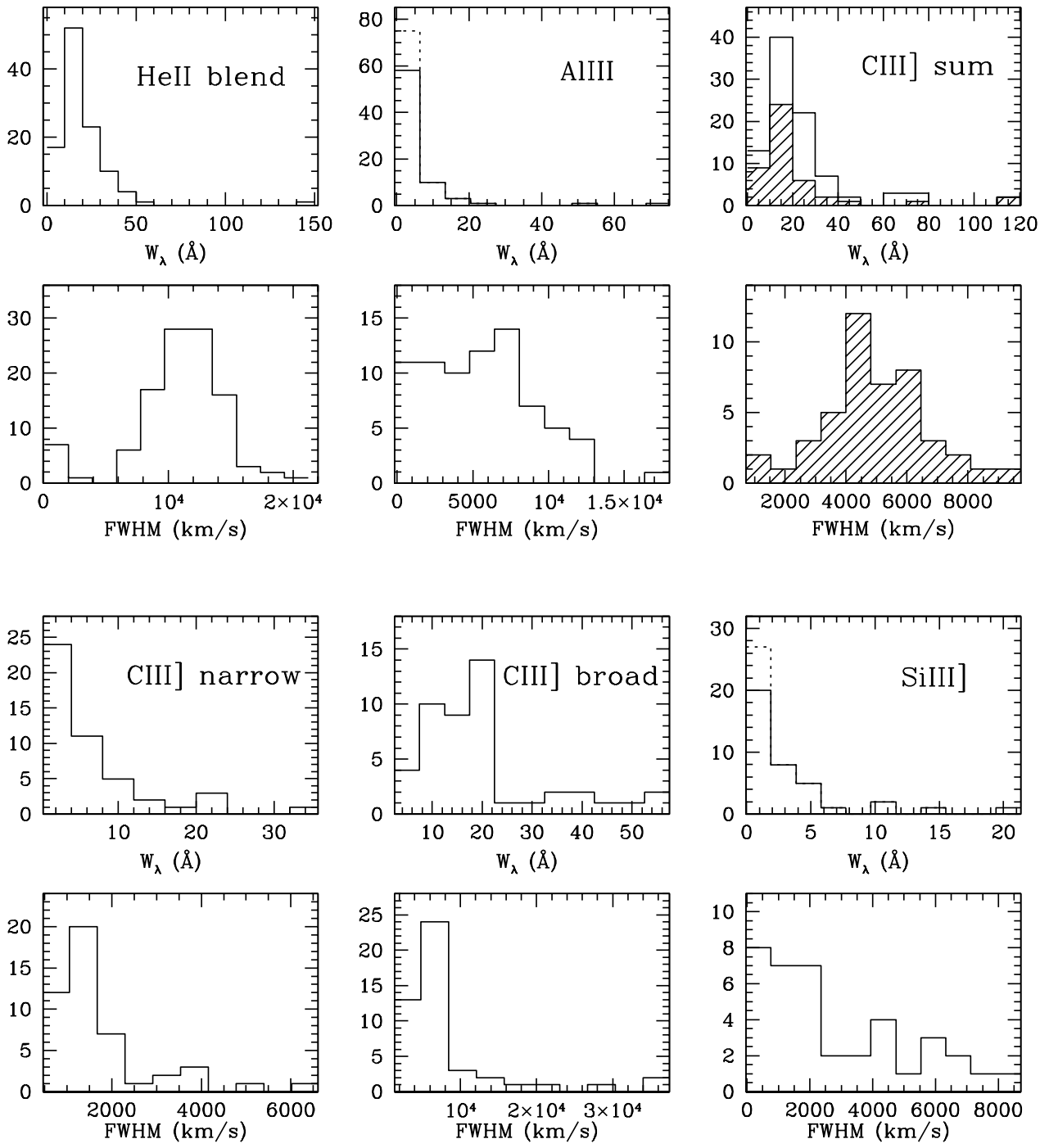

FIG. 2.—*Continued*

We also looked at the correlations between $L(2500\ \text{Å})$ and the broad and narrow components of strong emission lines. We find that both the narrow and the broad components of Lyα and C IV show significant BEff with the probability of a chance correlation in the Cox, Kendall, and Spearman tests less than 0.01%, while C III] shows a marginal correlation for the narrow component ($P = 0.02/0.00/0.01$ in Cox/Kendall/Spearman tests, respectively) and an even weaker trend for the broad component ($P = 0.11/0.06/0.07$). The BEff for the narrow component is stronger than for the broad component in all these lines (Spearman's ρ for Lyα is -0.476 and -0.411, for C IV is -0.523 and -0.510, and for C III] is -0.372 and -0.272, for the narrow and broad components, respectively). This is consistent with Francis et al. (1992) and Osmer, Porter, & Green (1994) who found, performing the spectral principal component analysis on the LBQS spectra, that most variance in the spectra is caused by the change in emission line cores. However, adding the broad and narrow components, and analyzing the line as a whole does not add scatter to the BEff. The probability of the BEff correlation occurring by chance is smaller (or the amplitude of Spearman's ρ is larger) for the sum of the narrow and broad components than for the narrow or broad components

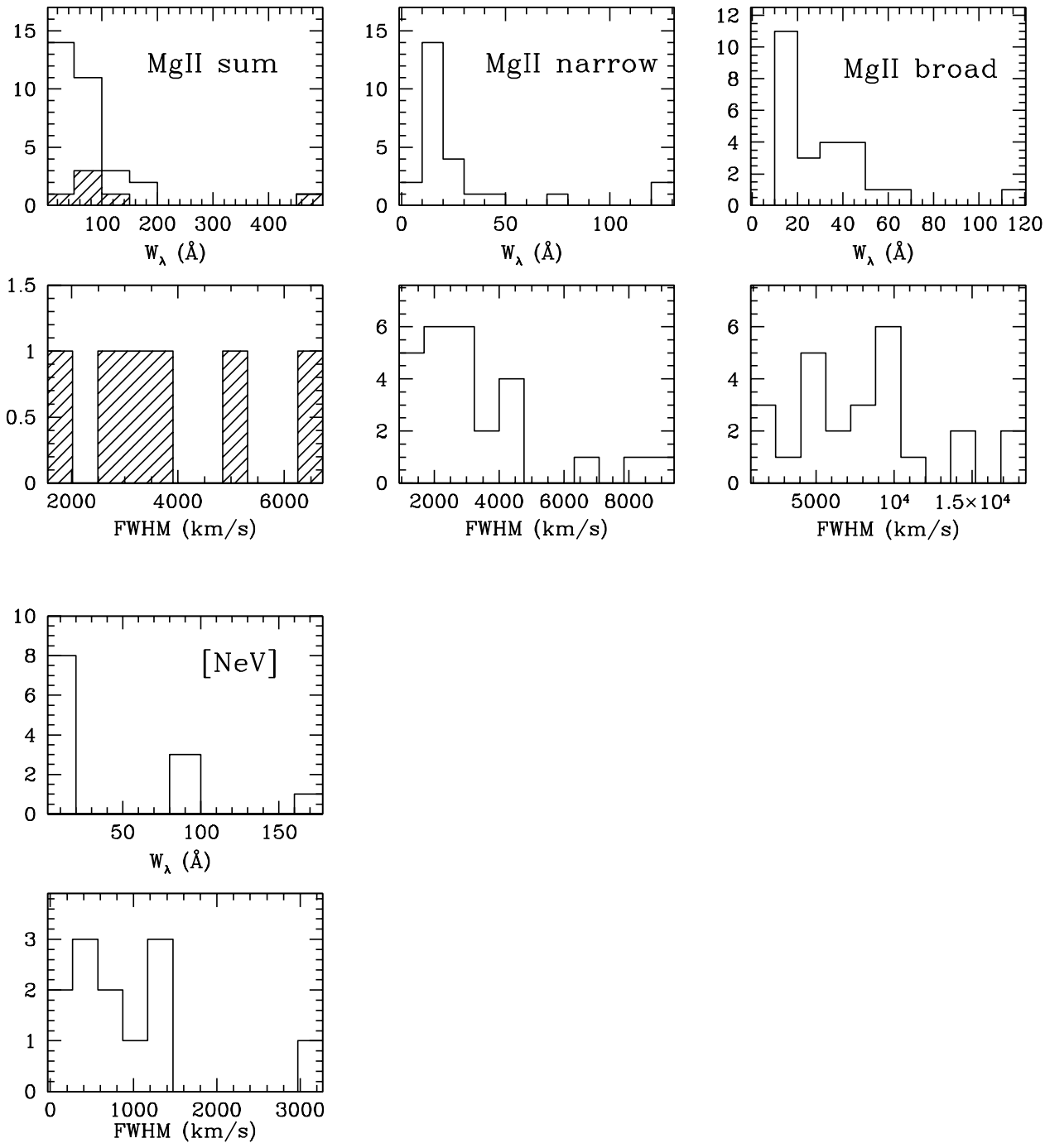

FIG. 2.—*Continued*

analyzed separately (Spearman's ρ for Lyα sum is -0.494, for C IV sum is -0.524, and for C III] sum is -0.372).

7.2. *Evolution*

We find significant correlations between the line equivalent widths and redshift for: Fe UV, Lyα, Si IV, C IV, He II, Si III], C III], and a weak trend for Lyβ and Al III (see Table 8 for the chance probabilities, slopes, and intercepts of the evolution regressions). We also examine, following the LBQS analysis, whether the primary (stronger) correlations are with z or L using the Partial Spearman Rank Analysis (see Green et al. 2001 for details). For Fe UV and the blended lines of Si IV, He II, Al III, Si III], and C III] the primary correlations are with redshift (see Table 9). However, for other emission lines—Lyβ, Lyα, N V, O I, C IV, and Mg II—the primary correlations are with luminosity. The LBQS analysis, which showed that *all* the emission lines correlated more strongly with redshift than with luminosity, implied that an evolutionary effect could be the cause of the BEff. However, the LBQS is a magnitude-limited sample ($16.0 \leq m_{B_J} \leq 18.85$) where the L-z correlation is extremely strong, making it difficult to disentangle

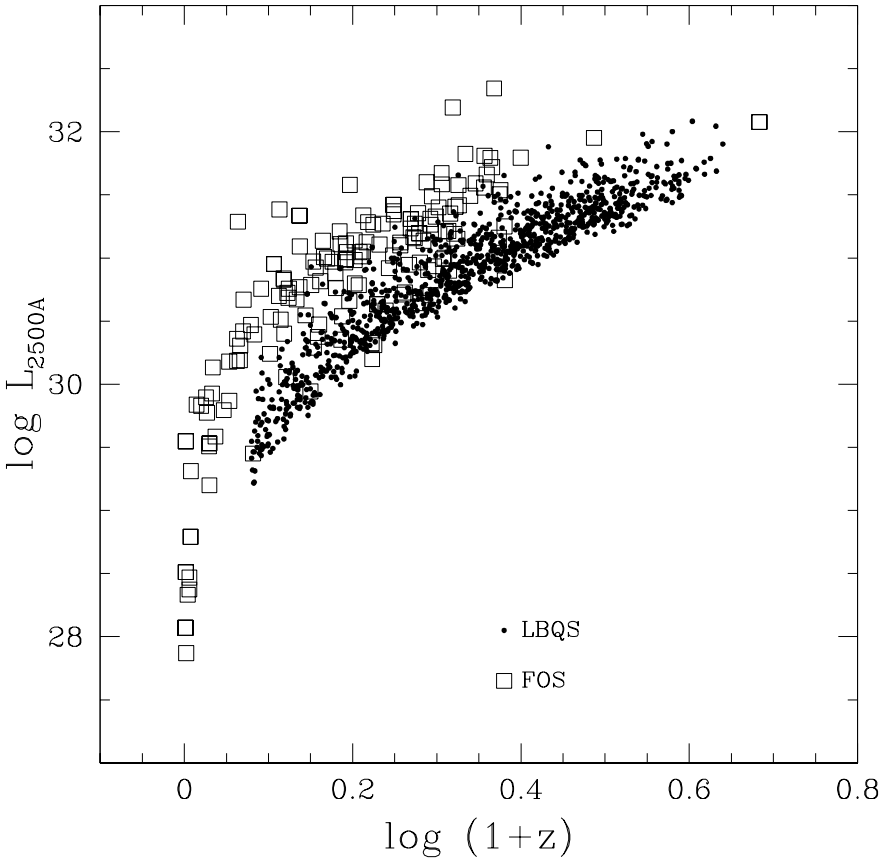

FIG. 3.—Luminosity vs. redshift in the FOS and the LBQS samples. Open squares represent FOS AGNs, dots the LBQS quasars.

between the luminosity and evolutionary effects. The analysis of the more heterogeneous FOS sample, which has a better coverage of the *L*-*z* plane (see Fig. 3), shows that the primary correlations with redshift found in the LBQS sample for the strong emission lines are possibly due to the LBQS being magnitude limited. However, for Fe UV and Si IV lines the primary correlations are with redshift both for the LBQS alone and the FOS sample (and also when FOS+LBQS samples are analyzed together) and probably is a real effect. Whether this also applies to the He II, Al III, Si III], and C III] lines is more difficult to answer, as these lines are heavily blended: He II is a blend of six lines (see Appendix), and although we do our best to deblend the C III] + Si III] + Al III complex, any conclusions for these individual lines may be tenuous.

TABLE 7

BALDWIN EFFECT REGRESSIONS

EMISSION LINE			ALL DATA (INCLUDING UPPER LIMITS)			DETECTIONS ONLY		
Line Name	Total	Limits	C/K/S [a]	Slope	Intercept	C/K/S [a]	Slope	Intercept
Fe UV	84	21	0.03/0.05/0.05	-0.102 ± 0.061	4.22 ± 1.87	0.02/0.00/0.00	-0.091 ± 0.023	4.30 ± 0.65
Fe Optical	9	1	0.10/0.29/0.28	-0.258 ± 0.099	8.71 ± 2.83	0.90/0.80/0.82	-0.095 ± 0.420	4.34 ± 11.83
O VI + Lyβ	96	2	0.00/0.00/0.00	-0.260 ± 0.064	9.09 ± 1.97	0.00/0.00/0.00	-0.257 ± 0.068	9.00 ± 2.14
Lyα	141	0	0.00/0.00/0.00	-0.137 ± 0.019	6.14 ± 0.60	0.00/0.00/0.00	-0.137 ± 0.019	6.14 ± 0.60
N V	139	11	0.46/0.08/0.10	-0.046 ± 0.063	2.26 ± 1.92	0.00/0.03/0.04	-0.060 ± 0.055	2.81 ± 1.69
O I	132	12	0.02/0.02/0.03	-0.078 ± 0.030	2.61 ± 0.91	0.00/0.01/0.01	-0.097 ± 0.035	3.24 ± 1.04
Si IV	128	0	0.00/0.00/0.00	-0.150 ± 0.026	5.52 ± 0.79	0.00/0.00/0.00	-0.150 ± 0.026	5.52 ± 0.79
C IV	123	0	0.00/0.00/0.00	-0.145 ± 0.029	6.25 ± 0.87	0.00/0.00/0.00	-0.145 ± 0.029	6.25 ± 0.87
He II	109	2	0.04/0.00/0.00	-0.069 ± 0.037	3.29 ± 1.14	0.00/0.00/0.00	-0.064 ± 0.035	3.16 ± 1.08
Al III	91	17	0.54/0.55/0.47	-0.142 ± 0.070	4.60 ± 2.12	0.02/0.14/0.11	-0.127 ± 0.065	4.33 ± 2.00
Si III]	45	7	0.00/0.01/0.01	-0.203 ± 0.084	6.30 ± 2.55	0.01/0.02/0.02	-0.184 ± 0.084	5.82 ± 2.56
C III]	92	0	0.00/0.00/0.00	-0.104 ± 0.021	4.41 ± 0.63	0.00/0.00/0.00	-0.104 ± 0.021	4.41 ± 0.63
Mg II	33	2	0.31/0.27/0.28	-0.038 ± 0.052	2.76 ± 1.62	0.03/0.10/0.10	-0.085 ± 0.037	4.27 ± 1.11

NOTES.—Schmitt two-dimensional Kaplan-Meier regression fits and errors from ASURV. The Baldwin effect examined here is $\log L(2500\ \text{Å}) \propto \log W_\lambda(\text{line})$.

[a] Probability of a correlation occurring by chance from ASURV for (C) Cox proportional Hazard model, (K) generalized Kendall's tau, and (S) Spearman's ρ tests.

TABLE 8
EVOLUTION REGRESSIONS

EMISSION LINE			ALL DATA (INCLUDING UPPER LIMITS)			DETECTIONS ONLY		
Line	Total	Limits	C/K/S [a]	Slope	Intercept	C/K/S [a]	Slope	Intercept
Fe UV	85	22	0.08/0.00/0.01	-0.195 ± 0.070	0.999 ± 0.116	0.01/0.00/0.00	-0.187 ± 0.035	1.399 ± 0.067
Fe Optical	9	1	0.12/0.32/0.29	-0.116 ± 0.306	1.211 ± 0.788	0.90/0.89/0.89	-0.076 ± 0.321	1.461 ± 0.800
O VI + Lyβ	97	2	0.27/0.02/0.03	-0.202 ± 0.124	0.946 ± 0.045	0.37/0.01/0.02	-0.241 ± 0.119	0.957 ± 0.025
Lyα	143	0	0.00/0.00/0.00	-0.167 ± 0.028	1.864 ± 0.026	0.00/0.00/0.00	-0.167 ± 0.028	1.864 ± 0.026
N V	141	11	0.96/0.36/0.38	0.007 ± 0.118	0.849 ± 0.068	0.01/0.08/0.08	-0.058 ± 0.099	0.917 ± 0.055
O I	134	13	0.14/0.08/0.11	-0.056 ± 0.051	0.188 ± 0.059	0.01/0.04/0.05	-0.090 ± 0.068	0.217 ± 0.048
Si IV	129	0	0.00/0.00/0.00	-0.233 ± 0.053	0.818 ± 0.035	0.00/0.00/0.00	-0.233 ± 0.053	0.818 ± 0.035
C IV	125	0	0.00/0.00/0.00	-0.198 ± 0.036	1.724 ± 0.048	0.00/0.00/0.00	-0.198 ± 0.036	1.724 ± 0.048
He II	110	2	0.01/0.00/0.00	-0.108 ± 0.049	1.139 ± 0.034	0.00/0.00/0.00	-0.119 ± 0.069	1.140 ± 0.043
Al III	91	17	0.06/0.00/0.00	-0.459 ± 0.114	0.015 ± 0.104	0.01/0.00/0.00	-0.310 ± 0.088	0.276 ± 0.088
Si III]	45	7	0.00/0.00/0.00	-0.375 ± 0.180	-0.117 ± 0.127	0.01/0.01/0.01	-0.298 ± 0.215	0.016 ± 0.157
C III]	92	0	0.00/0.00/0.00	-0.236 ± 0.029	1.122 ± 0.034	0.00/0.00/0.00	-0.236 ± 0.029	1.122 ± 0.034
Mg II	33	2	0.45/0.98/0.80	0.016 ± 0.162	1.640 ± 0.129	0.04/0.41/0.52	-0.170 ± 0.053	1.534 ± 0.084

NOTES.—Schmitt two-dimensional Kaplan-Meier regression fits and errors from ASURV. The relations examined here are $\log W_\lambda(\text{line}) \propto \log z$.
[a] Probability of a correlation occurring by chance from ASURV for (C) Cox proportional Hazard model, (K) generalized Kendall's tau, and (S) Spearman's ρ.

7.3. *Baldwin Effect and Evolution Slopes*

All the FOS BEff slopes are significantly flatter than in the LBQS. This finding is consistent with the Netzer, Laor, & Gondhalekar (1992) model in which the Baldwin effect is caused by geometrically thin, optically thick accretion disc with a viewing angle dependent optical/UV emission and an isotropic line emission. A sample of objects with differing disk luminosities and inclination angles produces, in this model, a Baldwin effect slope dependent on the luminosity range of the sample, with flatter slopes expected for samples of larger luminosity range.

The slopes of the Lyα and C IV Baldwin effect are consistent with those found for a heterogeneous sample of *IUE* spectra studied by Kinney et al. (1990; 0.12 ± 0.05 for Lyα, and 0.17 ± 0.04 for C IV) and Espey & Andreadis (1999; 0.08 ± 0.03 for Lyα, and 0.17 ± 0.03 for C IV) as well as for a number of optically selected complete samples from Zamorani et al (1992; 0.13 ± 0.03 for C IV). Interestingly, the slopes of the evolution effect for all emission lines in the FOS (and FOS + LBQS) sample are also flatter than in the LBQS, resembling the behavior of the BEff slopes which flatten with increasing luminosity range.

We find a trend (chance probability of $\sim$4% in both Kendall and Spearman tests) of an anticorrelation between the ionization potential of the emission line and the slope of the BEff, with the slope of the BEff slopes of -0.0013 ± 0.0003 (see Fig. 4). This trend, first found by Espey & Andreadis (1999), is consistent with BEff being caused by the change of AGN spectral energy distribution (SED) with luminosity. The emission lines with higher ionization potential are expected, in this picture, to show steeper BEff slopes due to a greater difference between the higher energy line-producing continuum and that measured underneath the line.

TABLE 9
PARTIAL CORRELATIONS OF LOG W_λ

	ALL DATA (INCLUDING UPPER LIMITS)				DETECTIONS ONLY			
	log L(2500 Å)		log z		log L(2500 Å)		log z	
LINE	P	ρ	P	ρ	P	ρ	P	ρ
UV iron	0.217	0.090	0.023	−0.221*	0.366	0.044	0.011	−0.293*
Lyβ	<0.005	−0.334*	0.034	0.192	<0.005	−0.322*	0.054	0.170
Lyα	<0.005	−0.275*	>0.400	0.016	<0.005	−0.275*	>0.400	0.016
N V	0.037	−0.155*	0.125	0.101	0.108	−0.111*	0.392	0.024
O I	0.043	−0.152*	0.228	0.067	0.019	−0.193*	0.194	0.084
Si IV + O IV]	>0.400	−0.009	0.016	−0.193*	>0.400	−0.009	0.016	−0.193*
C IV	<0.005	−0.242*	0.287	−0.051	<0.005	−0.242*	0.287	−0.051
He II	>0.400	−0.011	0.046	−0.163*	0.316	−0.047	0.131	−0.113*
Al III	<0.005	0.465	<0.005	−0.543*	0.015	0.260	<0.005	−0.387*
Si III]	>0.400	−0.011	0.086	−0.214*	>0.400	0.003	0.096	−0.221*
C III]	<0.005	0.317	<0.005	−0.538*	<0.005	0.317	<0.005	−0.538*
Mg II	<0.005	−0.484*	<0.005	0.455	0.013	−0.411*	0.045	0.317

NOTES.—P, partial Spearman rank probability; ρ, partial correlation coefficient of a W_λ correlation occurring by chance, where W_λ depends on two variables log L(2500 Å) and log z, and the partial correlation is calculated while holding one of the variables constant. For each line the primary (stronger) correlation is denoted by an asterisk (*) on ρ.

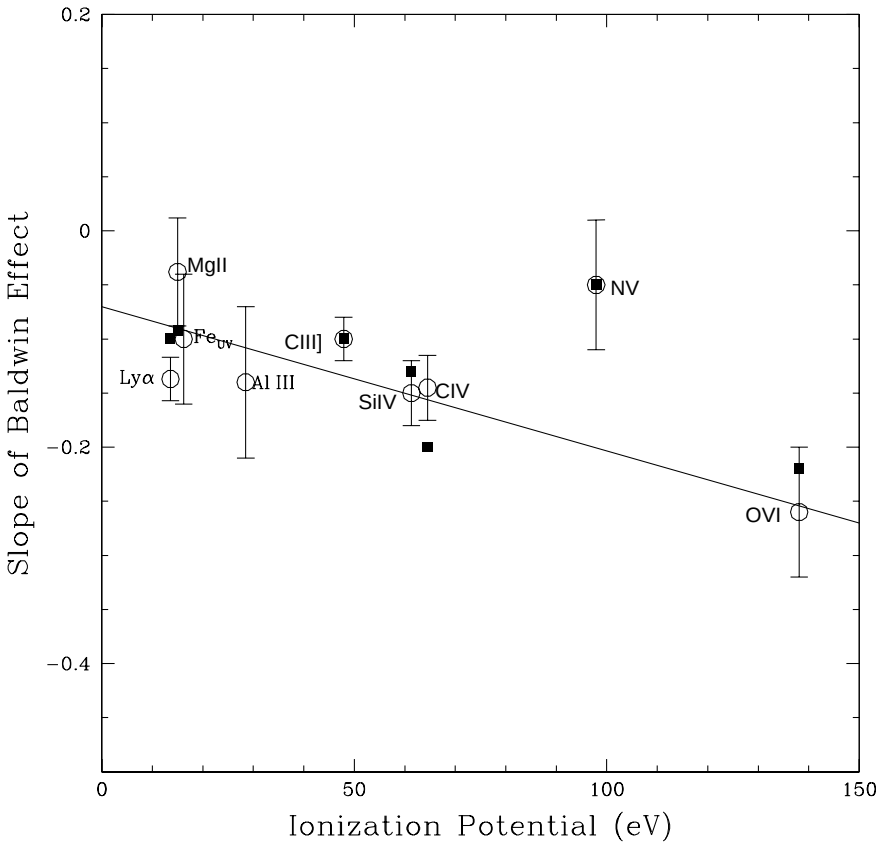

FIG. 4.—Dependence of the slope of the Baldwin Effect on the ionization parameter of the emission line in the FOS sample. The filled squares are the slopes predicted by the LOC model of Korista et al.

Korista, Baldwin, & Ferland (1998) have calculated emission line fluxes using a "locally optimally emitting cloud (LOC)" model in which clouds with a large range of densities, sizes, and distances from the ionizing continuum source compose the broad emission line region, where those clouds with the optimal physical parameters for emission in a given line contribute the most flux. When the clouds are illuminated by a model power law with a changing continuum slope, the LOC model predicts the BEff slopes shown as filled squares in Figure 4. These slopes are generally consistent with the slopes we find in the FOS sample, confirming that the SED change is the likely cause of the BEff.

All the above analysis of the slope of BEff slopes has been made by ignoring the N v BEff slope, which is much flatter than all the other emission line slopes. It is, however, consistent with the Korista et al. prediction, if the BEff flat slope is due to the metallicity increase in high-redshift/luminosity quasars (Hamann & Ferland 1993).

8. CONCLUSIONS

In this paper we present the emission line properties of 158 AGNs (174 spectra) observed by FOS/*HST* before the installation of COSTAR. Using an automated technique, which accounts for galactic extinction, blended iron emission, and galactic and intrinsic absorption lines, we uniformly measure the equivalent widths, FWHM, and peak shifts relative to the systemic redshift of the UV/optical emission lines spanning from Lyβ to Hα. The measurements are quoted with errors, and upper limits to equivalent widths are estimated where emission lines are undetected. The FOS spectra, together with the 993 LBQS spectra from Paper I, comprise the largest emission line database wherein emission and absorption lines have been uniformly measured.

In this paper we study the relation between emission line equivalent widths and UV luminosity in the FOS sample. We find a significant Baldwin effect for Lyβ, Lyα, Si IV, He II, C IV, and C III] and a previously unreported Si III] Baldwin effect. We find that narrow components of Lyα, C IV, and C III] show a stronger Baldwin effect than the broad components, consistent with the spectral principal component analysis which showed that most variance comes from emission line cores (Francis et al. 1992; Osmer et al. 1994). We also find a Baldwin effect in UV iron, significant when both FOS and LBQS samples are analyzed together. The values of the Baldwin effect slopes and the dependence of the slopes on the sample's luminosity range point to a change of the SED as the cause of the Baldwin effect in the FOS sample.

We also study the relations between the line equivalent widths and redshift and find significant anticorrelations for Fe UV, Lyα, Si IV, C IV, He II, Si III], and C III] and trends for Lyβ and Al III. For UV iron and weak or blended lines (Si IV, He II, Al III, Si III], C III]) stronger (primary) correlations are with redshift, while for other emission lines (Lyβ, Lyα, N V, O I, C IV, Mg II) the primary correlations are with luminosity. This is inconsistent with the LBQS sample, where *all* emission lines correlated more strongly with redshift than with luminosity. We conclude that the primary

correlations with redshift in the LBQS sample may be due to the LBQS sample being magnitude limited.

This database will become useful in a number of projects, vital for the understanding of the physics of the broad emission line region. The large range of redshifts and luminosities covered by the FOS + LBQS sample [$0 < z < 3.0$, and $10^{28} < L(2500\ \text{Å}) < 10^{32}$ ergs s^{-1}] will, for example, enable tests for the dependence of abundances (estimated from the N v/C iv, N v/He ii line ratios—Hamann & Ferland 1993) on luminosity or redshift. Correlations between abundances and continuum properties such as luminosity, radio-loudness, or UV/X-ray continuum shape will give clues to the factors driving the enrichment of gas in the BLR. The FOS absorption line measurements can be used to measure the frequency of UV absorption in AGNs, whether it depends on luminosity of the AGN, and whether it is consistent with the X-ray absorption (confirmed only in Seyfert 1 galaxies, see Crenshaw et al. 1999). Finding a relation between intrinsic UV absorption lines and continuum properties (e.g., Brandt, Laor, & Wills 2000 find stronger UV absorption for weaker soft X-ray QSOs) will help assess the physics of the absorbing gas, its location and origin. Finally, the relation of any emission line property or line ratio with the width of the BLR lines will give clues to the dependence of the BLR properties on the black hole mass (since black hole mass $\propto \text{FWHM}^2$ assuming BLR cloud motions are virialized).

The authors gratefully acknowledge support provided by NASA through grant NAG5-6410 (LTSA). This work has made use of the NASA/IPAC Extragalactic Database (NED) which is operated by the Jet Propulsion Laboratory, California Institute of Technology, under contract with the National Aeronautics and Space Administration. Based on observations made with the NASA/ESA *Hubble Space Telescope*, obtained from the data archive at the Space Telescope Science Institute. STScI is operated by the Association of Universities for Research in Astronomy, Inc., under the NASA contract NAS 5-26555.

APPENDIX

A1. NOTES ON EMISSION LINES

Lyβ + O vi λ1035.—The spectrum near this emission line blend was modeled with a flat "pseudo" continuum and a single Gaussian, since Lyβ and O vi are so closely blended. The resulting equivalent width should be treated as approximate.

He ii λ1640.—The region on the red side of C iv λ1549 includes emission from a number of lines including He ii λ1640, [Ne v] $\lambda\lambda$1575, 1593, [Ne iv] $\lambda\lambda$1602, 1609, Si ii λ1650, [O iii] $\lambda\lambda$1661, 1663, 1668, and Al ii λ1670. However, we model this region with a single He ii Gaussian component, as the use of multiple Gaussian components did not improve the model fit. The true value of He ii line parameters (particularly the FWHM) is likely to be significantly smaller than quoted in Table 5.

[Ne v] λ3426, [O ii] λ3728, [Ne iii] λ3869.—These lines lie on top of the Balmer continuum which was not accounted for during the global power-law continuum fit. Hence, we measured the lines above a local continuum, defined as the power-law fit to 30 Å wide continuum windows on the red and blue side of each emission line.

A2. NOTES ON INDIVIDUAL SPECTRA

0010+1058ra.—This spectrum consists of two spectra that do not overlap and are simply joined to form a single spectrum.

0027+2241ra.—Blue end of the G190H spectrum is noisy and was ignored below 1630 Å before merging.

0420−5456ra.—Not a good continuum fit to 4000–4800 Å region; for a better Hα fit, an intermediate Hα component was introduced in addition to the narrow and broad components.

0743−6726ra.—Heavily absorbed O vi.

0837+4450ra.—A gap in spectrum at C iv line.

0847+3445ra.—Spectrum consists of two spectra, which do not overlap but have similar flux level and are simply joined.

0927+3902ra, rb.—Spectrum ends at Mg ii.

0956+4115ra.—Blue end of the G190H spectrum is noisy and was ignored below 1605 Å before merging.

1003+6813ra.—Heavily absorbed O vi and Lyα.

1004+2855ra.—Blue end of the G190H spectrum is noisy and was ignored below 1605 Å before merging (note that this region lies on Lyα); the region at 1516–1523 Å was ignored due to second-order grating reflection effect.

1011+1304ra.—Heavily absorbed O vi and Lyα.

1048−2509ra.—Strong Galactic absorption in Mg ii.

1139+6547ra.—G150L spectrum was ignored above 1650 Å due to a low S/N.

1208+4540ra.—Heavily absorbed O vi and Lyα.

1210+3924rb, 1210+3924rc.—Heavily absorbed Lyα and C iv.

1219+0638ra.—Blue end of the G190H spectrum is noisy and was ignored below 1605 Å before merging; note that this region lies on Lyα.

1225+3332ra.—Galactic absorption contaminating C iv and Mg ii.

1229+0203ra.—The strong absorption feature at 1209–1223 Å does not appear in all spectra that were merged; this may be due to oversubtraction of geocoronal Lyα in some of these spectra; we exclude this region from further analysis. Also, there is no overlap in the constituent spectra around 1600–1650 Å, leaving a break at the Si iv + O iv.

1231−0224ra.—Spectrum ends at Lyα.

1244+1721ra.—Heavily absorbed O vi.

1259+3423ra.—Strong absorption in O vi.

1301+5902ra.—Blue end of the G190H spectrum is noisy and was ignored below 1605 Å before merging.
1341+4123ra.—Heavily absorbed O VI and Lyα.
1342+6021ra.—Heavily absorbed Lyα and C IV.
1354+0052ra.—Heavily absorbed Lyα.
1357+1919ra.—Blue end of the G190H spectrum is noisy and was ignored below 1605 Å before merging.
1417+2508rb.—A merger of 40 spectra of NGC 5548, which is known to have variable luminosity and emission line profiles.
1524+0958ra.—Heavily absorbed O VI and Lyα.
1620+1736ra.—Gratings change at O VI.
1634+7031ra.—Heavily absorbed O VI.
1704+6044ra.—Blue end of the G190H spectrum is noisy and was ignored below 1605 Å; heavily absorbed O VI, Lyα.
1719+4804ra.—Heavily absorbed O VI and Lyα.
1821+6420ra.—Blue end of the G190H spectrum is noisy and was ignored below 1605 Å before merging.
2044−1043ra.—Strong NAL absorption in Lyα.
2137−1432ra.—Strong NALs in Lyα and C IV.
2218−0335ra, rb, rc.—Gratings change at Lyα.
2303−6807ra.—Gratings change at O VI.

The following spectra were fitted with continuum consisting of two power laws, which were joined at 4200 Å rest frame: 0242−0000ra, 0242−0000rb, 0420−5456ra, 0615+7102ra, 1048−2509ra, 1214+1403ra, 1230+1223rA, and 1230+1223rB. However, in 1210+3924ra discontinuous optical and UV power laws provide a better fit to the UV part of the spectrum. The normalization of the optical power law at 4220 Å rest frame is $7.439^{+0.001}_{-0.001}$.

REFERENCES

Aldcroft, T. A. 1993, Ph.D. thesis, Stanford Univ.
Alexander, T., & Netzer, H. 1994, MNRAS, 270, 781
Baldwin, J. A., Wampler, E. J., & Gaskell, C. M. 1989, ApJ, 338, 630
Boroson, T. A., & Green, R. F. 1992, ApJS, 80, 109 (BG92)
Brandt, W. N., Laor, A., & Wills, B. J. 2000, ApJ, 528, 637
Brotherton, M. S., Wills, B. J., Francis, P. J., & Steidel, C. C. 1994, ApJ, 430, 495
Cardelli, J. A., Clayton, G. C., & Mathis, J. S. 1989, ApJ, 345, 245
Crenshaw, D. M., Kraemer, S. B., Boggess, A., Maran, S. P., Mushotzky, R. F., & Wu, C.-C. 1999, ApJ, 516, 750
Dietrich, M., & Wilhelm-Erkens, U. 2000, A&A, 354, 17
Elvis, M., Wilkes, B. J., & Lockman, F. J. 1989, AJ, 97, 77
Espey, B., & Andreadis, S. 1999, in ASP Conf. Ser. 162, Proc. Quasars as Standard Candles for Cosmology, ed. J. Baldwin & G. J. Ferland (San Francisco: ASP), 351
Ferland, G. J., Baldwin, J. A., Korista, K. T., Hamann, F., Carswell, R. F., Phillips, M., Wilkes, B. J., & Williams, R. E. 1996, ApJ, 461, 683
Forster, K., Green, P. J., Aldcroft, T., Vestergaard, M., & Foltz, C. B. 2001, ApJS, 134, 35 (Paper I)
Francis, P. J., Hewett, P. C., Foltz, C. B., & Chaffee, F. H. 1992, ApJ, 398, 476
Freeman, P., Doe, S., & Siemiginowska, A. 2001, Proc. SPIE, 4477, 76
Gehrels, N. 1986, ApJ, 303, 336
Green, P. J., Forster, K., & Kuraszkiewicz, J. K. 2001, ApJ, 556, 727 (Paper II)
Hamann, F., & Ferland, G. J. 1993, ApJ, 418, 11
Heiles, C., & Cleary, M. N. 1979, Australian J. Phys. Astrophys Supp., 47, 1
Isobe, T., Feigelson, E. D., & Nelson, P. I. 1986, ApJ, 306, 490
Keyes, C. D., Koratkar, A. P., Dahlem, M., Hayes, J., Christiansen, J., & Martin, S. 1995, Faint Object Spectrograph Instrument Handbook, version 6.0 (Baltimore: STSci)
Kinney, A. L., Rivolo, A. R., & Koratkar, A. P. 1990, ApJ, 357, 338
Koratkar, A., & Gaskell, C. M. 1991, ApJ, 345, 637
Korista, K., Baldwin, J., & Ferland, G. 1998, ApJ, 507, 24
Krolik, J. H., & Kallman, T. R. 1988, ApJ, 324, 714
Laor, A., Fiore, F., Elvis, M., Wilkes, B. J., & McDowell, J. C. 1994, ApJ, 435, 611
———. 1997, ApJ, 477, 93
Lavalley, M., Isobe, T., & Feigelson, E. D. 1992, in ASP Conf. Ser. 25, Astronomical Data Analysis Sortware and Systems I, ed. D. M. Worral, C. Biemsderfer, & J. Barnes (San Francsico: ASP), 245
Lockman, F. J., & Savage, B. D. 1995, ApJS, 97, 1
Marziani, P., Sulentic, J. W., Dultzin-Hacyan, D., Calvani, M., & Moles, M. 1996, ApJS, 104, 37
Murray, N., & Chiang, J. 1998, ApJ, 494, 125
Netzer, H., & Davidson, K. 1979, MNRAS, 187, 871
Netzer, H., Laor, A., & Gondhalekar, P. M. 1992, MNRAS, 254, 15
Osmer, P. S., Porter, A. C., & Green, R. F. 1994, ApJ, 436, 678
Perry, J. J., & Dyson, J. E. 1985, MNRAS, 213, 665
Stark, A. A., Gammie, C. F., Wilson, R. W., Bally, J., Linke, R. A., Heiles, C., & Hurwitz, M. 1992, ApJS, 79, 77
Veron-Cetty, M.-P., & Veron, P. 1996, Catalog of Quasars and Active Galactic Nuclei (7th ed.; Garching: ESO)
Vestergaard, M., & Wilkes, B. J. 2001, ApJS, 134, 1
Wilkes, B. J., Kuraszkiewicz, J., Green, P. J., Mathur, S., & McDowell, J. C. 1999, ApJ, 513, 76
Wills, B. J., Laor, A., Brotherton, M. S., Wills, D., Wilkes, B. J., Ferland, G. J., & Shang, Z. 1999, ApJ, 515, L53
Zamorani, G., Marano, B., Mignoli, M., Zitelli, V., & Boyle, B. J. 1992, MNRAS, 256, 238
Zheng, W., Kriss, G. A., & Davidsen, A. F. 1995, ApJ, 440, 606
Zheng, W., & Malkan, M. A. 1993, ApJ, 415, 517